Lake Surface Area Forecasting Using Integrated Satellite-SARIMA-Long-Short-Term Memory Model

Keyvan Soltani
Razi University
Arash Azari
Razi University
Mohammad Zeynoddin
Laval University: Universite Laval
Afshin Amiri
University of Tehran
Isa Ebtehaj
Laval University: Universite Laval
Taha B.M.J. Ouarda
Institut national de la recherche scientifique
Bahram Gharabaghi
University of Guelph
Hossein Bonakdari (hossein.bonakdari@fsaa.ulaval.ca)
Universite Laval https://orcid.org/0000-0001-6169-3654

Research Article

Keywords: Water resources, stochastic model, SARIMA, Tashk-Bakhtegan Lakes, hybrid model, forecasting.

DOI: https://doi.org/10.21203/rs.3.rs-631247/v1

Lake Surface Area Forecasting Using Integrated Satellite-SARIMA-Long-Short-Term Memory Model

Keyvan Soltani[1], Arash Azari[2], Mohammad Zeynoddin[3], Afshin Amiri[4], Isa Ebtehaj[3], Taha B.M.J. Ouarda[5], Bahram Gharabaghi[6], Hossein Bonakdari[3, *]

[1]Department of Civil Engineering, Razi University, Kermanshah, Iran

[2]Department of Water Engineering, Razi University, Kermanshah, Iran

[3]Department of Soils and Agri-Food Engineering, Université Laval, Québec, Canada, G1V 0A6

[4]Department of Remote Sensing and GIS, University of Tehran, Tehran, Iran

[5]Institut National de la Recherche Scientifique, Centre Eau Terre Environnement, INRS-ETE, Québec, G1K 9A9 Canada

[6]School of Engineering, University of Guelph, Guelph, Ontario NIG 2W1, Canada

[*]Corresponding author, Phone: +1 418 656-2131, Fax: +1 418 656-3723, E-mail: hossein.bonakdari@fsaa.ulaval.ca

Abstract

Lake Water Surface Area (WSA) plays a vital role in environmental preservation and future water resource planning and management. Accurately mapping, monitoring and forecasting Lake WSA changes are of great importance to regulatory agencies. This study used the MODIS satellite images to extract a monthly time series of WSA of two lakes located in Iran from 2001 to 2019. Following a consequence of image and time series preprocessing to obtain the preprocessed lake surface area time series, the outcomes were modeled by the Long-Short-Term Memory (LSTM) deep learning (DL) method, the stochastic Seasonal Auto-Regressive Integrated Moving Average (SARIMA) method and hybridization of these two techniques with the objective of developing WSA forecasts. After separate standardization and normalization of A_L TS and reevaluation of the preprocessed data, the SARIMA $(1, 0, 0)(0, 1, 1)_{12}$ model outperformed sole LSTM models with correlation index of (R) 0.819, mean absolute error (MAE) of 49.425 and mean absolute percentage error (MAPE) of 0.106. On the other hand, the hybridization (stochastic-DL) enhanced the reproduction of the primal statistical properties of WSA data and caused better mediation. However, the other accuracy indices did not change markedly (R 0.819, MAE 49.310, MAPE 0.105). The multi-step preprocessing and reevaluation also caused all LSTM models to produce their best results by less than 12 inputs.

Keywords: Water resources, stochastic model, SARIMA, Tashk-Bakhtegan Lakes, hybrid model, forecasting.

1. Introduction

Accurate mapping of lake Water Surface Areas (WSA) is essential to assess the amount of surface water available [1–5]. WSA is also helpful in determining the relationship between climate and water resources [6–9] and for assessing the impacts of changing water surfaces, which is crucial in water resources management [10-11]. The various methods for the extraction of water surface from remote sensing data fall into two general categories: single-band and multi-band techniques. The single-band technique uses a multispectral image band and identifies other ground-surface phenomena based on a threshold limit for water sources. The multi-band method helps distinguish the water masses from the differences in the reflectance properties of different bands [12]. Monitoring the water dynamics with images taken at different times can show changes in lakes, reservoirs and flood surfaces [13, 14].

Google Earth Engine (GEE) comprises a considerable amount of satellite and global data types worldwide, making it possible to analyze this data for various purposes such as change detection [15] , mapping [16, 17] and ground level studies [18]. GEE has been widely used in a number of disciplines including reviewing global forest changes [19], estimating crop production [20], ground subsidence monitoring [21], coral reef mapping [22], modeling global surface water change [23, 24], flood risk assessment [25], global urban mapping [26, 27], renewable energy mapping [28], drought monitoring [29], and the reconstruction of the MODIS global vegetation index [30].

Satellite data have been commonly used in hydrological studies [31–35, 36]. Nath and Deb [37] used satellite images to detect and extract the water body of Puyang China. Abou El-Magd and Ali [38] studied surface evaporation from Lake Nasser using high-resolution radiometer satellite images. They demonstrated that robust assessments of lake evaporation can be obtained. Song et al. [39] studied water level and lake area in the Tibetan Plateau by extracting time series from Landsat images. Moreira et al. [34] investigated and modelled water balance using satellite images and the evapotranspiration dataset in South America. Veh [40] developed an algorithm to detect the glacial lake outburst floods (GLOFs) in the Himalayas. The algorithm uses satellite images to analyze GLOFs and provide interpretable statistics for risk assessment and hazard prevention planning.

The pace of artificial intelligence (AI) models' development and their accuracy is rapidly increasing nowadays. These models are increasingly utilized in various fields of science, including water engineering and hydrology [41–43], since these models produced acceptable results in modelling sophisticated time series. Also, developments in AI and the computer industry played an important role [44] in accelerating this pace. In this field, deep learning methods produced noticeable results in modelling and forecasting hierarchical data [45-47]. The most recent deep learning model, LSTM, can utilize the unlimited historical raw data as inputs to detect the structure of the data and forecast future steps. The LSTM method is widely used in many fields like natural language understanding and speech recognition [48], image and text survey [49], hydrological data modelling such as precipitation and runoff forecasting [42,50], and modeling climatic and meteorological data [51]. Mohan and Gaitonde [52] used LSTM to model turbulent flow control and its temporal dynamics. Murad and Pyun [53] employed LSTM alongside support vector machine (SVM) and k-nearest neighbours (KNN) for human activity recognition, and they reported a higher performance of the LSTM model compared to other types of AI models. Sahoo et al. [54] used LSTM recurrent neural networks (LSTM-RNN) to model low flow hydrological time series. With a 94 percent correlation and low errors, they reported an acceptable potential of LSTM for modelling hydrological time series.

Stochastic methods are among the most renowned statistical models. These methods are popular amongst researchers because of their comprehensible principles and easy application. Seasonal Auto-Regressive Integrated Moving Average (SARIMA) uses non-seasonal and seasonal parameters to forecast time series based on historical data linearly [55–58]. Papalaskaris et al. [59] employed the SARIMA model for short-term basin rainfall forecasting in Kavala City, Greece. Mombeni et al. [60] used SARIMA for estimating one-year-ahead water demand in Iran. However, most hydrological time series have complex structures that cannot be efficiently modeled by linear methods like stochastic models or by AI models. Hence, some researchers resorted to the integration of AI and linear models to utilize both their capabilities. Hybridization of AI and linear models is one method that helps catch the complexity in time series and which has produced more accurate results [35,61–64]. Mishra et al. [65] employed a combination of stochastic SARIMA model and ANN to predict droughts in the Kansabati River basin in India. The results indicated that a hybrid model leads to higher accuracy. Shafaei et al. [66] applied wavelet pre-processing to SARIMA, ANN and hybridization of both and modelled monthly precipitation in Iran. They indicated that wavelet-SARIMA-ANN produces better results than wavelet-SARIMA and wavelet-ANN.

A novel methodology based on the integration of remote sensing and deep learning- stochastic modelling for lake surface area forecasting is proposed in the present work. To the best knowledge of the authors, no previous studies have attempted to use such hybrid model for WSA. The satellite images are downloaded, pre-processed and digitized for each time point to obtain changes in the water area. Then the achieved time series is modelled and forecasted by three methods. The modelling methods are deep learning LSTM model, stochastic SARIMA and hybridization SARIMA-LSTM. Prior to modelling, the time series structure is analysed by stationarity and normality tests and other statistical and visual tests. If any pre-processing is needed, a standardization and/or normalization of the series is carried out to obtain the optimized modelling results. In the end, statistical and visual tools survey the methods presented in the methodology.

2. Material and Methods

2.1. Case study

The Tashk-Bakhtegan lakes (TB lakes) with a surface area of 540 km^2 are Iran's second-largest inland lakes. These lakes are the most important ecological habitats of Iran at an altitude of 1525 m above sea level and have a catchment area of 25,000 km^2. The maximum depth of Tashk-Bakhtaran lake is 2 m, and the maximum depth of Tashk lake is 3.1 m [66, 67]. These lakes are located between 29° 13'N–29° 48'N and 54° 10'E–53° 23'E. Water inflows to these lakes through the Kor and Syvand rivers. With the construction of three dams in these rivers' upper basin, the inflow of water into these lakes has decreased dramatically, causing a large area to dry out [68]. Fig.1 shows the location of the twin TB lakes in Iran.

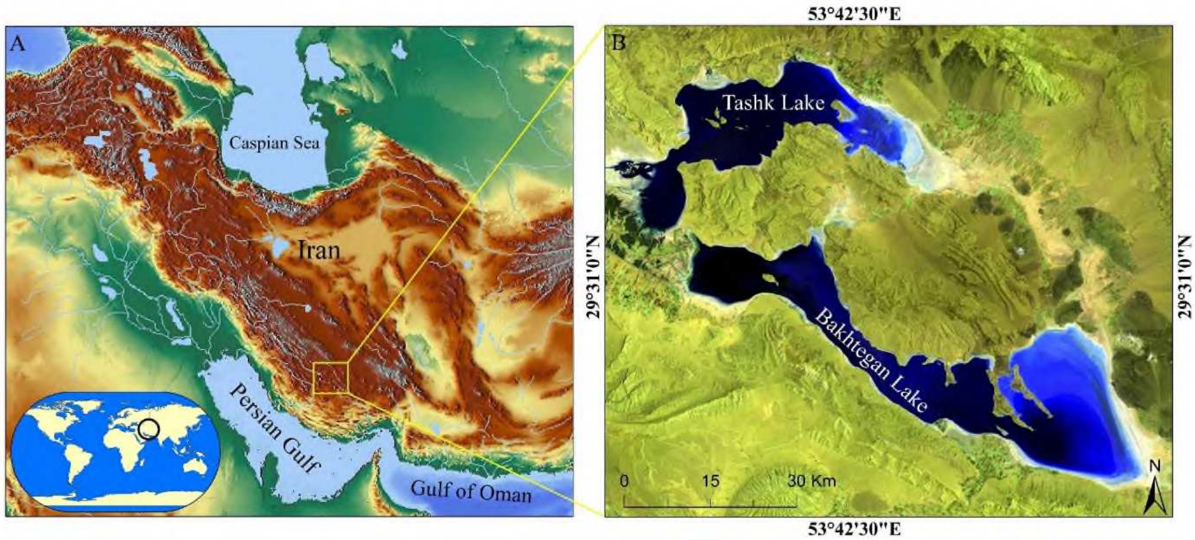

Fig. 1. A) Geographic location of the study area, B) Landsat 5 TM satellite image of TB lakes in false colour composite (7,4,1).

Arid and semi-arid regions cover about one-third of the world's land area.. Population growth in such areas caused an increase in the harvesting of groundwater [69]. In arid regions, lakes and wetlands play an indispensable role in the region's ecosystem, including climate change modification and food resources provision in the area. Due to growing water consumption in arid regions, water resources such as lakes ground water and other aquatic ecosystems are increasingly under stress [68].

TB lakes are under threat of complete drought due to over-harvesting of groundwater and mismanagement. In the basin of these lakes, two large rivers, Kor and Sivand, flow. Due to the vast area of TB lakes and moisture and water availability, unique plant and animal habitats exist in the surroundings [70]. In the past, TB lakes had a more fertile environment than today due to proper nutrition. At least 220 species of plaants have been identified in the region's environment (the third largest from the species number point of view in Iran). More than 100,000 waterfowl migrate to the region in the winter [71]. There were about 5,000 Marbled Duck in 1990 [71,72]. Due to the diversity of flora and fauna in the wildlife, a refuge and a national park have been identified as protected areas. Their location is shown in Fig. 2. Three important dams that have been built in the upstream area of TB lakes: Sivand dam, Mollasadra dam and Doroodzan (Dariush) dam. The location of these dams is specified in Fig. 2, and their specifications are shown in Table 1.

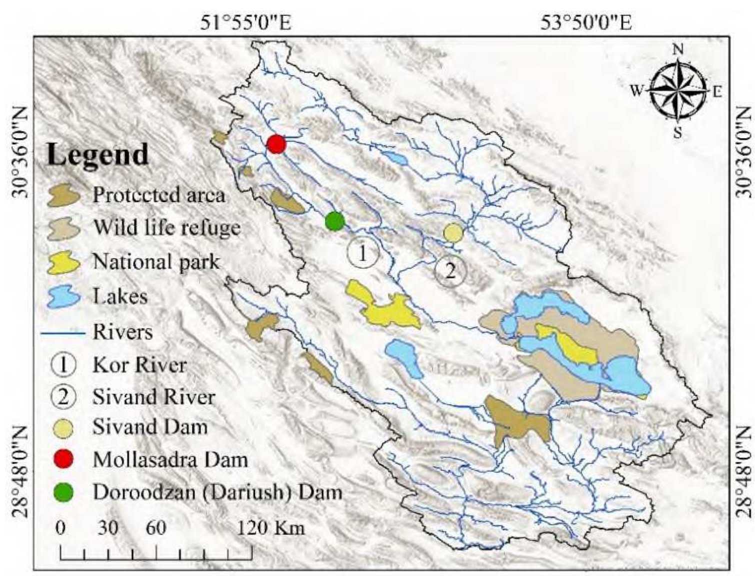

Fig. 2. TB lakes watershed and location of ecological areas and distribution of dams in the area.

Table 1. Characteristics of dams located upstream of TB lakes.

Dam	River	H.[1](m)	Vol.[2] (M.m^3)	Year[3]	Dam Type
Doroodzan	Kor	85	960	1972	A pebble with an impermeable core
Mollasadra	Kor	75	440	2007	Reservoir (soil with clay core)
Sivand	Sivand	57	255	2007	Soil with clay core

1. Height; 2. Total tank volume (million cubic meters); 3. Year of operation

In Fig. 3 using MODIS satellite, the land cover changes in 2001 and 2018 are compared. This figure was provided using the MODIS Land Cover Type Product (MCD12Q1) satellite. The MCD12Q1 includes a global dataset of land cover types from 2001 to 2018. Its spatial resolution is 500 meters, and six different classification schemes have been used to produce it. The Global Earth Coverage Map provides ecological and physical characteristics of the Earth's surface.

In this study, LC_Type 1 band was employed to prepare a land cover map of the areas around TB lakes. This ground cover is based on the International Geosphere-Biosphere Program (IGBP), which is dedicated to styding global changes. The annual land cover maps around TB lakes were extracted from MCD12Q1 data in 2001 and in 2018 and are presented in Fig. 3. The reduction of agricultural coverage, pastures, and water level of the lake in the catchment area of TB lakes and the increase of barrier surface are clearly visible.

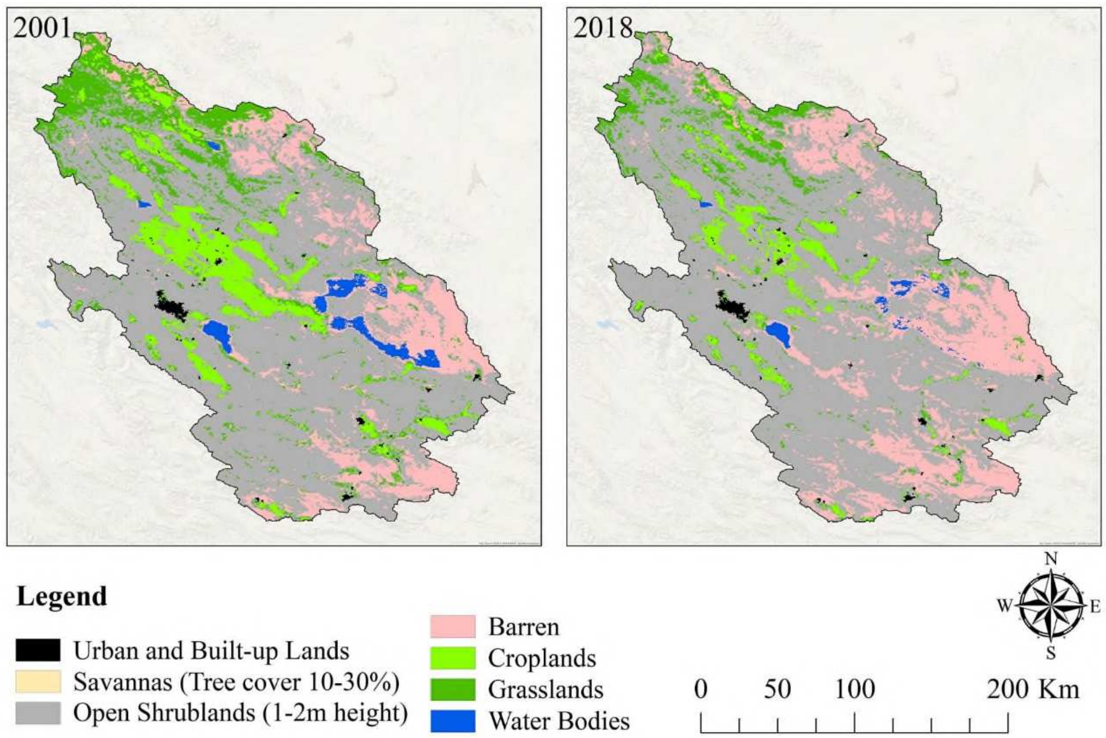

Fig. 3. Map of land cover changes between 2001 and 2018 in TB lakes watershed.

Fig. 4 shows the changes in five variables: Open shrublands, Grasslands, Barren, Croplands, and Water Bodies between 2001 and 2018. It can be observed that the area covered by Open Shrublands has been relatively stable until 2007, but since 2007, it has been increasing, while grasslands and croplands have declined with a similar trend.

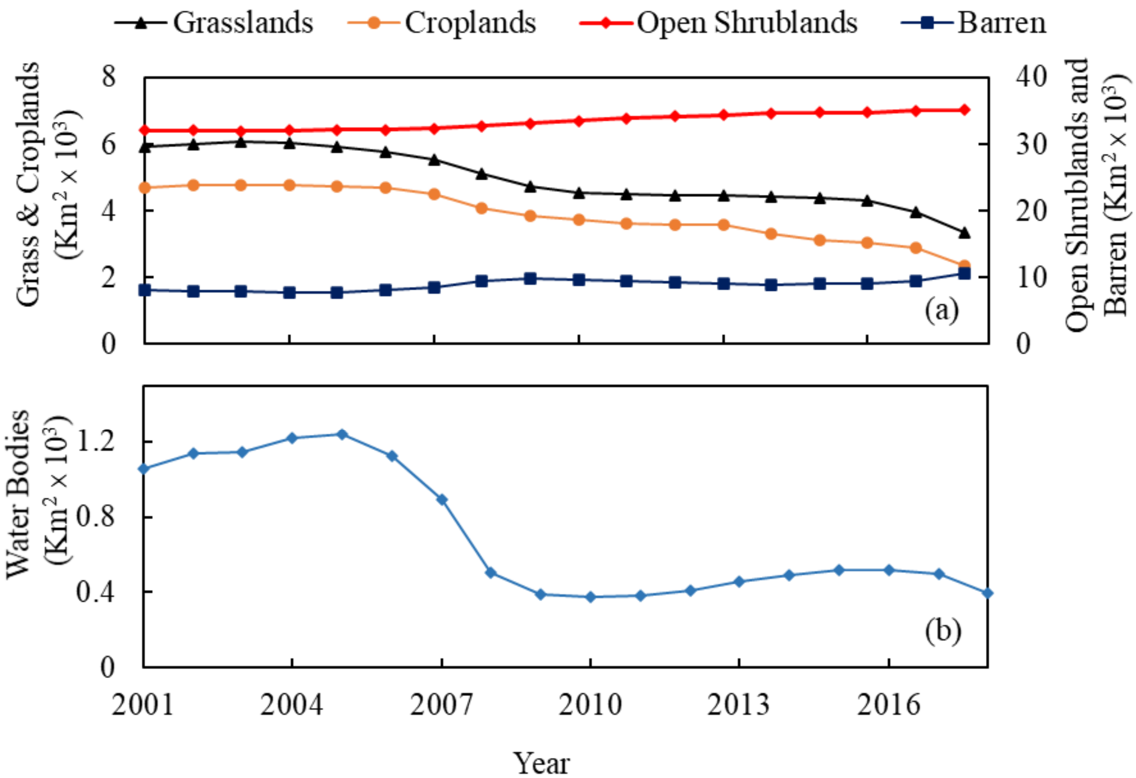

Fig. 4. a) Land cover changes in 2001-2018, b) changes in TB lakes area.

Charts seem to indicate the existence of sudden changes around 2006 and 2007, particularly in the Waterbody area, which has declined since 2007 and reached its lowest surface in 2009. This reduction has had significant effects on other uses in the region. It should be noted that this decrease in water bodies in the catchment area of TB lakes has started since the construction of two dams, Mollasadra dam and Sivand dam, i.e., in 2007, and in 2009. These two dams were constructed on the two main rivers of the region, which feed the TB lakes, and resulted in the reduction of these lakes surfaces. Due to the diversity of flora and fauna in the region and protected areas around the TB lakes, these dams have caused severe damage to these genetic resources and the uses of the region. TB lakes increase the humidity of the air, and due to the high altitude of the surrounding mountains, the resulting moisture remains in the atmosphere of the same area. This is referred to as artificial irrigation and causes better fruiting of the plants in this area.

The drought that has been observed in recent years and the significant reduction of TB lakes' water have affected the region's uses and caused a water crisis in the region. Croplands and grasslands have shown a significant decline, with their area shrinking to less than half its original value. Simultaneously, Shrublands and Barren soils increased, resulting in falling water levels in the region and the release of agricultural land and land-use change due to the lack of water in the area.

Considering all this background information, the question is raised on how long will the drought process of TB lakes continue, and what will be the changes in their surface in the coming years? To answer this question, we adopt the SARIMA-Long-Short-Term Memory Model to model the lake's surface changes and provide a practical model for future changes in the lake's surface. Hence, using this model, an applied plan for water resources management in a variety of uses in the region can be developed, reducing the water crisis in the region and the abandonment of agricultural land, which has severe environmental and economic consequences in the region.

2.2. Remote sensing (RS) datasets and pre-processing

The MODIS (Moderate Resolution Imaging Spectroradiometer) tools were launched by Terra and Aqua satellites in 1999 and 2002. The MODIS sensor captures images 2230 kilometres wide and generates complete coverage of the earth in 1-2 days. By using Surface Reflectance products and their various bands (MOD09A1), the spectral reflectance of Earth's surface is estimated.

Pre-processing is a vital part of the remote sensing process. One of the problems with remote sensing images is the presence of clouds. Therefore, tools and indices like Google Earth Engine Environment (GEE) for image classification and the NDWI index are required to obtain desirable results. The NDWI index is one of the most commonly used indicators in remote sensing and is calculated from the relationships between bands (equations 1 and 2). Bands are used to obtain the water in which wavelengths have the highest and lowest spectral reflections. The NDWI relationship is computed as follows [73]:

$$NDWI = \frac{G - NIR}{G + NIR} \tag{1}$$

where the G is the green band, and the NIR is the near-infrared band. The modified NDWI relationship is as follows [12]:

$$MNDWI = \frac{G - MIR}{G + MIR} \tag{2}$$

where MIR is the mid-infrared band (wavelengths 1.2 to 2.2 μm).

The resulting image of the MNDWI index has values between -1 and +1. The pixels that indicate the presence of water have positive values. However, due to the presence of mixed pixels that cause errors in the detection of water sources, a threshold limit ($MNDWI \geq 0.3$) is used to detect pure pixels with more precision [74,75]. Then, to calculate the area of water bodies in the images, the number of pure pixels identified in each image is multiplied by the area of land cover and the exact area of the water surface can be calculated.

2.3. Time series and pre-processing

A series of measurements in equal time intervals is termed time series. Each time series has a stochastic and a deterministic part. Periodical patterns, trends and jumps are the deterministic part and can exist in time series simultaneously or solely. The absence of this part in time series is called stationarity state. For any modeling, the deterministic terms can be removed, and only the stochastic part is required. Therefore, analysis methods are needed to assess the predictable pattern in time series and stationarity [76]. Applying tests to time series to extract interpretable statistics is the analysis of time series. Tests like KPSS, Mann-Whitney, Mann-Kendal, and Jarque-Berra can be employed to investigate stationarity, jump, trends and normality of time series, respectively.

In the KPSS [77] test, a regression equation is fitted to the data. If the variance of the independent variables of the relationship is null the A_L, then the series is stationary. The KPSS relationship for trend or level stationarity is as follows:

$$A_L = r_t + \beta_t + \varepsilon_t \tag{3}$$

$$S^2(t_l) = \frac{1}{n}\sum_{t=1}^{n} e_t^2 + \frac{2}{n}\sum_{j=1}^{l} w\left(j, t_l\right)\frac{1}{n}\sum_{t=j+1}^{n} e_t e_{t-s} \tag{4}$$

$$w\left(s, t_l\right) = 1 - j/\left(t_l + 1\right) \tag{5}$$

$$KPSS = \frac{1}{n^2}\left(\sum_{t=1}^{N} \frac{S_t^2}{S^2\left(t_l\right)}\right) \tag{6}$$

where $S_t = \Sigma e_t$, t_l is the truncation lag, e_t are the residuals. $r_t = r_{t-1} + u_i$ and r_t is a random walk, u_i are independent variables with equal distribution with mean zero and variance σ^2, β_t is the deterministic term of the trend, and ε_t the stationarity error.

In the case of non-stationarity, causing factors are investigated. Trend as a non-stationarity factor is analyzed by the Mann-Kendal test as follows [78]:

$$\operatorname{stnd}(M_T) = \begin{cases} (M_T - 1)\operatorname{var}(M_T)^{-0.5} & MK > 0 \\ 0 & MK = 0 \\ (M_T + 1)\operatorname{var}(M_T)^{-0.5} & MK < 0 \end{cases} \tag{7}$$

where stnd (M_T) is the standard of Mann-Kendall statistic, MK is the Man-Kendall statistic, and var (M_T) is the variance of M_T. The M_T and var (M_T) are defined as:

$$M_T = \sum_{i=1}^{N-1} \sum_{j=i+1}^{N} \operatorname{sgn}\left(A_{L,j} - A_{L,i}\right) \tag{8}$$

$$\operatorname{var}(M_T) = \left(\left(2N^3 - 7N^2 - 5N\right) - \sum_{j}^{g} A_{L,j}\left(A_{L,j} - 1\right)\left(2L_{L,j} + 5\right)\right)/18 \tag{9}$$

where $A_{L,j}$ and $A_{L,i}$ are the lake area time series at the j[th] and i[th] group, g is the number of identical groups, sgn is the sign function, N is the number of samples and $L_{L,j}$ is the number of the observations at the jth group. The following equation is used for seasonal changes over time, or seasonal trend:

$$S_k = \sum_{i=1}^{N_k - 1} \sum_{j=i+1}^{N_k} \operatorname{sgn}\left(A_{L,kj} - A_{L,ki}\right) \tag{10}$$

$$M_{S_k} = \sum_{k=1}^{\omega}\left(S_k - \operatorname{sgn}\left(S_k\right)\right) \tag{11}$$

$$\operatorname{var}\left(M_{S_k}\right) = 2\sum_{i=1}^{\omega-1} \sum_{j=i+1}^{\omega} \sigma_{ij} + \sum_{k}\left(2N^3{}_k - 7N^2{}_k - 5N_k\right)/18 \tag{12}$$

$$\mathrm{stnd}\,(M_{S_k}) = M_{S_k}\ \mathrm{var}\left(M_{S_k}\right)^{-0.5} \tag{13}$$

where ω represents the seasons, k is the number of months, and σ_{ij} is the covariance of stationary test in seasons i and j. A probability corresponding to a test statistic higher than 5% means that A_L is trendless.

Jumps, the second non-stationarity factor, represent sudden steps in the time series. The non-parametric Mann-Whitney (MW) test is used to evaluate this factor [79, 80]:

$$\mathrm{MW} = \sum_{t=1}^{N_t}\left(\mathrm{Dg}\left(A_{L,\ \mathrm{Ordered}}\right) - \frac{N_{m1}\left(N_{m1}+N_{m2}+1\right)}{2}\right) / \left(\left(N_{m1}N_{m2}\left(N_{m1}+N_{m2}+1\right)\right)^{0.5}/12\right) \tag{14}$$

where $A_{L,\ \mathrm{Ordered}}$: series sorted by main series A_L, Dg ($A_{L,\ \mathrm{Ordered}}$) the degree of $A_{L,\ \mathrm{Ordered}}$ function, N_{m1} and N_{m2} is the number of members of the main sub-series that $N_{m1} + N_{m2} = N_{total}$. A probability related to a test statistic greater than 1% means that A_L is jump-less.

Periodicity as the third deterministic factor can be surveyed by a time series graph or the auto correlation function (ACF) and the partial auto correlation function (PACF) plots. This term appears as iterative sinusoidal variations in both above graphs.

Seasonal standardization is one of the conventional stationarizing methods in hydrology. This method also reduces jumps in time series [81]. By removing the seasonal mean and standard deviation, the A_L is transferred to a time series with a zero mean and a standard deviation equal to one as follows:

$$\mathrm{std}\omega = \left(A_L\left(t,\omega\right) - \bar{A}_L\left(\omega\right)\right) / S_d\left(\omega\right) \tag{15}$$

where, stdω represents the outcome of seasonal standardization, $A_L(t,\omega)$ is the sample at t^{th} year and the ω^{th} season, $\bar{A}_L(\omega)$ is the mean of the ω^{th} season and $S_d(\omega)$ is the standard deviation of ω^{th} season.

2.4. Long-Short-Term Memory (LSTM) deep learning model

Deep learning models are subclasses of artificial intelligence (AI) models enhanced for non-linear sequence solving problems. A renowned deep learning model is the Long Short-Term Memory (LSTM) network. The LSTM architecture is well suited for modelling sequence data like time series and can learn long-term dependencies in series to forecast future steps. A simple LSTM memory block is presented in Fig. 5. The LSTM model is constituted of several gates that control the flow of information and affect the produced results. These gates are the input, the forget, and the output gates which control the data entering to memory blocks c_t, which should be forgotten, and which are permitted to continue to further processes.

LSTM conducts a mapping [43] from an input sequence x to an output sequence y using the next equations iteratively from $t = 1$ to $t = \tau$ with initial values $C_0 = 0$ and $h_0 = 0$:

$$f_t = \sigma\,(W_f A_{L,t} + U_f\, h_{t-1} + b_f) \tag{16}$$

$$\tilde{C}_t = \tanh\,(W_{\tilde{C}_t} A_{L,t} + U_{\tilde{C}_t} h_{t-1} + b_{\tilde{C}_t}) \tag{17}$$

where $A_{L,t}$ is the input of the vector at time t, and h_{t-1} is the hidden cell state at time $t-1$. The weight matrices are U, W for input-to-hidden, and hidden-to-hidden connections, respectively. f_t is a resulting vector with values in the range (0, 1), $\sigma(\cdot)$ represents the logistic sigmoid function and W_f, U_f and b_f define the set of learnable parameters for the forget gate. $\tilde{C}_t$ is an update vector with (-1, 1) range for the cell state which calculated form $A_{L,\,t}$, tanh (*) is the hyperbolic tangent and $W_{\tilde{C}_t}$, $U_{\tilde{C}_t}$ and $b_{\tilde{C}_t}$ are other sets of learnable parameters.

$$i_t = \sigma\,(W_i x_t + U_i h_t + b_i) \tag{18}$$

i_t is the forget gate with range (0,1). W_i, U_i and b_i are a set of learnable parameters, defined for the input gate. The results of Eqs. 16 to 18 lead to update the cell state:

$$c_t = f_t O c_{t-1} + t_t O \tilde{C}_t \tag{19}$$

where O denotes element-wise multiplication. The output gate, as the last gate, controls the cell state c_t.

$$o_t = \sigma(W_o x_t + U_o h_{t-1} + b_o) \tag{20}$$

where o_t is in the range (0, 1) and W_o, U_o and b_o are a set of learnable parameters, defined for the output gate. h_t is calculated as follows:

$$h_t = \tanh(c_t)\,O\,o_t \tag{21}$$

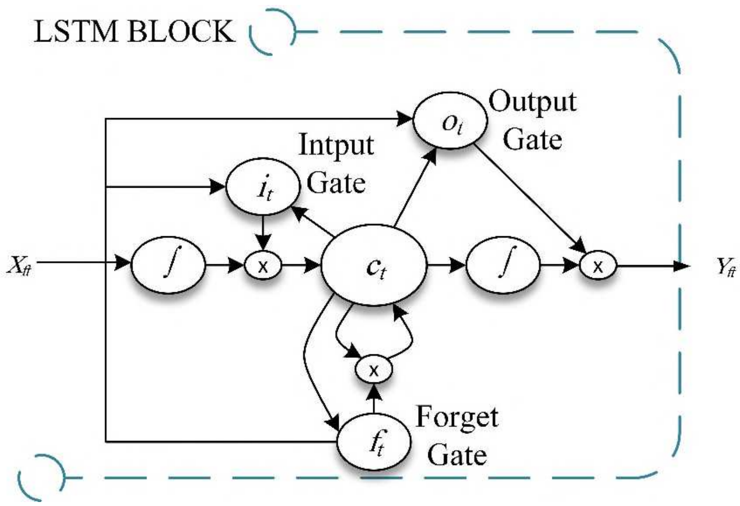

Fig. 5. A simple LSTM block.

2.5. Stochastic modelling concepts

Stochastic models are a subgroup of statistical models. These models are widely used in various fields of science beause of their simplicity of utilization and theory. Seasonal Auto-Regressive Integrated Moving Average (SARIMA) is a stochastic model with seasonal and non-seasonal parameters that allows the model to forecast the future by using historical data [82].

In a SARIMA (p, d, q) (P, D, Q) model, p and q are non-seasonal model parameters; P and Q are seasonal ones. d and D are the order of non-seasonal and seasonal differencing, respectively [83]. The simplified extension of the SARIMA equation for one step ahead forecast is as follows:

$$\begin{aligned}&(1-\varphi_1 L^1-\varphi_2 L^2-\ldots-\varphi_p L^p)\ (1-\Phi_1 L^{1\omega}-\Phi_2 L^{2\omega}-\ldots\ \Phi_P L^P)\ \left(1-L\right)^d (1-L^{\ \omega})^D A_L{}^{km^2}\left(t\right)\ldots\\&=(1-\theta_1 L^1-\theta_2 L^2-\theta_q L^q)\ (1-\Theta_1 L^{1\omega}-\Theta_2 L^{2\omega}-\ldots\ \Theta_Q L^{2Q})\, e\left(t\right)\end{aligned} \tag{22}$$

$$\varphi(B)\ \Phi(B)\ \left(1-L\right)^d (1-L^{\omega})^D A_L\left(t\right)=\theta(B)\Theta(B)\, e\left(t\right)$$

where ω is seasonality, φ and Φ are auto-regressive (AR) and seasonal AR (SAR) parameters, θ and Θ are the moving average (MA), L is the differencing operator $L(A_L(t)) = A_L(t-1)$. $(1-L)^d$ equals the d-th non-seasonal, and $(1-L^{\omega})^D$ equals the D-th seasonal with the lag ω. The L operator helps in modelling the non-stationary series as it removes correlations in time series and changes in mean and variance of the series. To improve the model's accuracy, each forecast is updated with real data, and a 1-step-ahead forecast is carried out. As this model is linear, deterministic terms must be extracted from the series, and data distribution normalized to improve accuracy. To evaluate the distribution's normality, the Jarque-Bera test can be applied to A_L time series [84]:

$$JB = n\left(S_k^2/6 + \left(K_u - 3\right)^2/24\right) \tag{23}$$

where K_u is kurtosis S_k is skewness; JB is a chi-square distribution with two degrees of freedom that can be used to assume that data is normal. As most of the hydrological time series are non-normal, normalizing transformation should be employed. John-Draper transform is a normalization approach that can transform A_L data. The equation is as follows:

$$A_{Ln}(\lambda) = \begin{cases} \operatorname{sgn}(A_L)\dfrac{\left(|A_L|+1\right)^{\lambda}-1}{\lambda} & \lambda \neq 0 \\ \operatorname{sgn}(A_L)\log\left(|A_L|+1\right) & \lambda = 0 \end{cases} \tag{24}$$

$$\operatorname{sgn}(A_L) = \begin{cases} 1 & A_L \geq 0 \\ -1 & A_L < 0 \end{cases} \tag{25}$$

λ is JD transforming parameters and A_{Ln} is the normalized A_L series.

2.6. Comparison measures

Correlation coefficient (R), Root mean squared error (RMSE), root mean squared relative error (RMSRE), Mean absolute percentage error (MAPE) and Mean absolute error (MAE) are used to evaluate the accuracy of models in time series obtained from pre-processing of A_L data. To compare the stochastic models, corrected Akaike's Information Criterion (AICc) is used. Theil's U coefficients are also used [85–87]. The Theil's U indices compare models based on the simplicity of the model against goodness-of-fit. The lower the index, the better the model results are.

$$R = \left(\frac{\left(\sum_{i=1}^{N} \left(A_{L,O,i} - \bar{A}_{L,O} \right) \left(A_{L,P,i} - \bar{A}_{L,P} \right) \right)}{\sqrt{\sum_{i=1}^{N} \left(A_{L,O,i} - \bar{A}_{L,O} \right)^2 \sum_{i=1}^{N} \left(A_{L,P,i} - \bar{A}_{L,P} \right)^2}} \right) \tag{26}$$

$$RMSE = \sqrt{\left(\sum_{i=1}^{N} \left(A_{L,O,i} - A_{L,P,i} \right)^2 \right) / N^2} \tag{27}$$

$$MAPE = \frac{100}{N} \sum_{i=1}^{N} \left(\frac{\left| A_{L,O,i} - A_{L,P,i} \right|}{A_{L,O,i}} \right) \tag{28}$$

$$MAE = \frac{1}{N} \sum_{i=1}^{N} \left(\left| A_{L,O,i} - A_{L,P,i} \right| \right) \tag{29}$$

$$RMSRE = \frac{1}{N} \sqrt{\sum_{i=1}^{N} \left(\frac{A_{L,O,i} - A_{L,P,i}}{A_{L,O,i}} \right)^2} \tag{30}$$

$$AICc = \frac{2kn + \left(n \ln(\sigma_{\varepsilon}^2)(n-k-1) \right)}{n-k-1} \tag{31}$$

$$U^{I} = \frac{\left[\sum_{i=1}^{N}\left(A_{L,O,i} - A_{L,P,i}\right)^{2}\right]^{0.5}}{\left[\sum_{i=1}^{N}\left(A_{L,O,i}\right)^{2}\right]^{0.5} + \left[\sum_{i=1}^{n}\left(A_{L,P,i}\right)^{2}\right]^{0.5}} \tag{32}$$

$$U^{II} = \frac{\left[\sum_{i=1}^{N} A_{L,O,i} - A_{L,P,i}{}^{2}\right]^{0.5}}{\left[\sum_{i=1}^{N}\left(A_{L,O,i}\right)^{2}\right]^{0.5}} \tag{33}$$

$A_{L,O,i}$ and $A_{L,P,i}$ are the i^{th} value of observed data and predicted A_L respectively. N is the number of months, σ_ε is the residual's standard deviation, and k is the number of tuned parameters through the modelling process. U^{I} is the accuracy of forecasting, and U^{II} is the forecasting quality. Checking the stochastic models' residuals for correlations and white noise state is one of the stochastic modelling steps. For this purpose, the Ljung-Box test can be applied to model residuals as follows [88]:

$$lbq = \left(N^{2} + 2N\right)\sum_{h=1}^{m}\frac{r_h}{N-1} \tag{34}$$

N is the number of samples, r_h is the residual coefficient of the autoregression (ε_t) in delay h; the value of m is also equal to ln(N). If the probability related to the Ljung-Box test is greater than the α-level (in this case $P_{lbq} > \alpha = 0.05$), the residues series is white noise.

In this research, first in the Google Earth Engine environment, the data were selected, and the necessary pre-processing was performed. MODIS MOD09A1 was used to measure the changes in the area of TB lakes. Images with a cloud coverage of less than 10% were selected to continue the process, and then the pixel value was corrected. Due to the area's characteristics, a threshold for water identification was considered, and with the MNDWI index, water bodies were separated from other zones. Higher threshold (MNDWI ≥0.3) was identified as water bodies. The time series of changes in the extent of the lakes was calculated from 2001 to 2019. Land cover changes were extracted from MODIS MCD12Q1, and the land cover map was prepared. To determine land use, the land cover map was used to identify the changes in the area and their impact on the changes in the lake surface. Then the time series of the WSA data was extracted from the satellite data. Following, the modelling procedure was undertaken.

Initially, the WSA time series' structural characteristics were investigated by pre-processed by stationarity and normality tests. If any pre-processing is needed, a standardization and/or normalization to series is carried out to obtain the optimized modelling results. Then deep learning LSTM model, stochastic SARIMA and hybridization SARIMA-LSTM are performed.. The described procedure is depicted in the flowchart of Fig. 6.

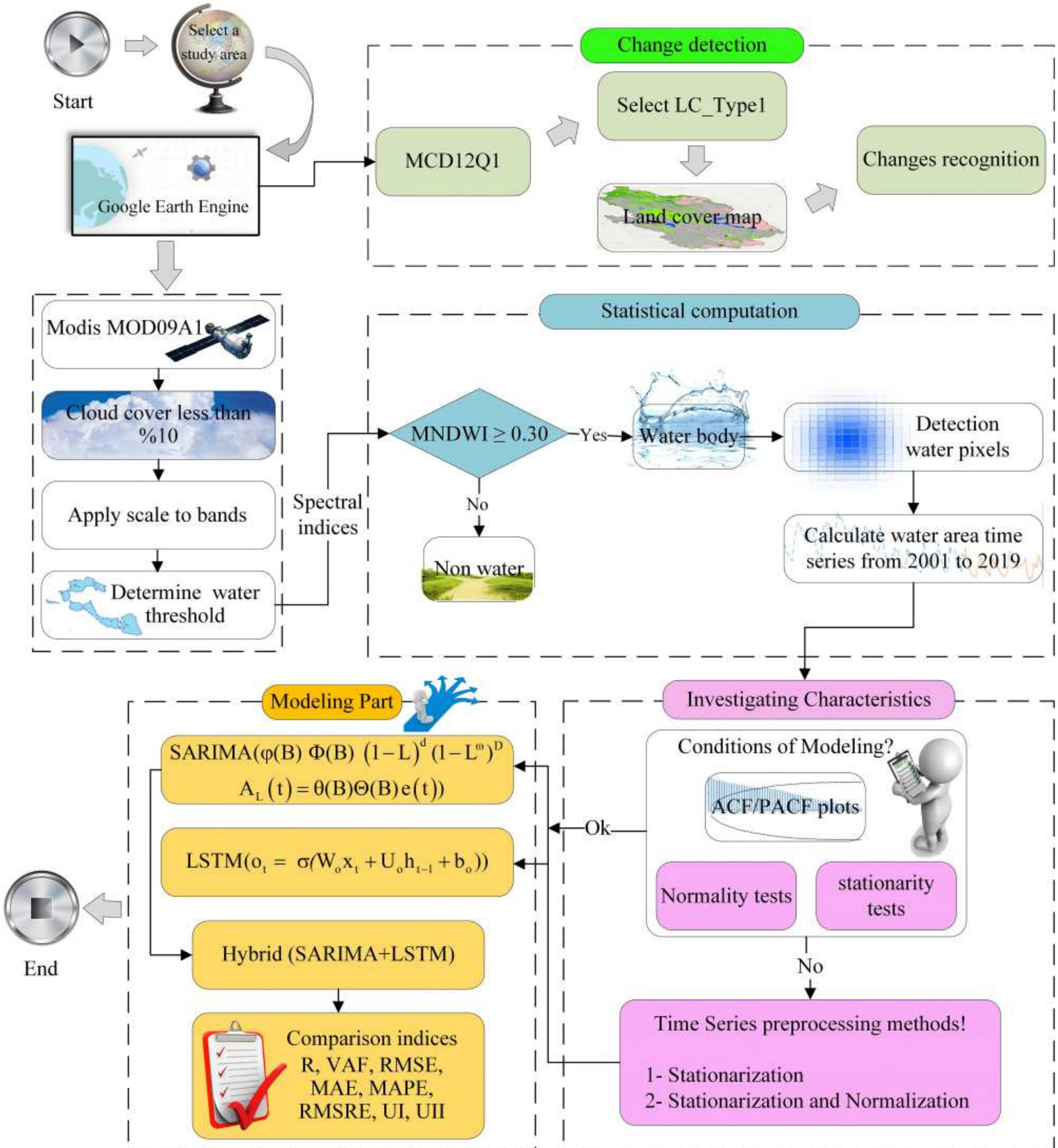

Fig. 6. Flowchart of the analytical procedures of the study.

3. Results and discussion

3.1. RS results

In this study, MODIS data, MOD09A1 version 6 Surface Reflectance (with a resolution of 500m and 8-day from 2000 to 2019) were employed to obtain time-series variations of TB lakes water surface. The MOD09 series is one of the MODIS surface reflection products. This product has seven bands and estimates the spectral reflectance values for each band in the absence of atmospheric absorption or diffusion.

Table 2 Specifications of MOD09A1 version 6

Band name	Band desc.	wavelength(nm)	Spatial resolution (m)
sur_refl_b01	S.R. Band 1	620-670	500
sur_refl_b02	S.R. Band 2	841-876	500
sur_refl_b03	S.R. Band 3	459-479	500
sur_refl_b04	S.R. Band 4	545-565	500
sur_refl_b05	S.R. Band 5	1230-1250	500
sur_refl_b06	S.R. Band 6	1628-1652	500
sur_refl_b07	S.R. Band 7	2105-2155	500

Band desc.: Band description; S.R. : Surface Reflectance

The necessary pre-processing, including atmospheric corrections, have been made to this product. The workflow for extracting the lake area from the MODIS images includes image preparation, image classification and statistical computation. During the preparation of the images, the location of the lakes was determined. So, at this point in the GEE Environment, images with more than 10% cloud were excluded from the lake extraction process. Images with cloud cover less than 10% were selected, and pixels suitable for classification were identified. The image classification step was also performed in the GEE environment. Fig. 7 illustrates the changes of A_L from 2001 to 2019 for April Month.

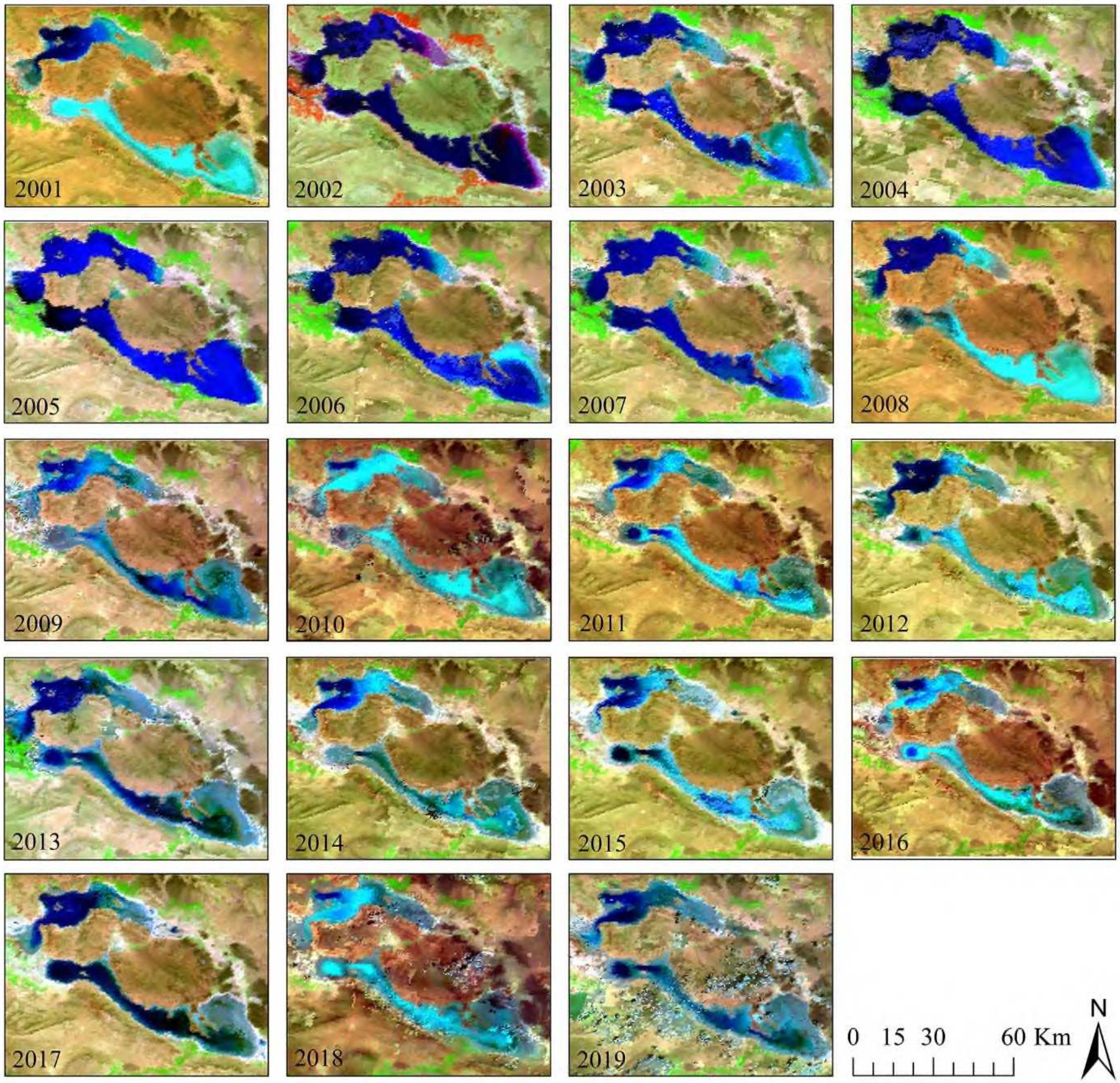

Fig. 7. Changes of A_L from 2001 to 2019 for April Month.

By using a function, the MNDWI index was applied to the previous step images. Water has high reflectance at the wavelength of 0.5 µm (green band) and absorbs electromagnetic waves at infrared wavelengths and has low reflectance. Therefore, in this study, band 4 (green band) and band 7 (mid-infrared) of MODIS images were used. After applying the threshold limit, the exact area of the water surface was obtained. For better change recognition in the lake surface area, the area has been separated from the surrounding environment, and the changes in the TB lakes based on this model are shown in Fig. 8. Based on the calculated areas, the monthly time series of the TB lakes area was achieved.

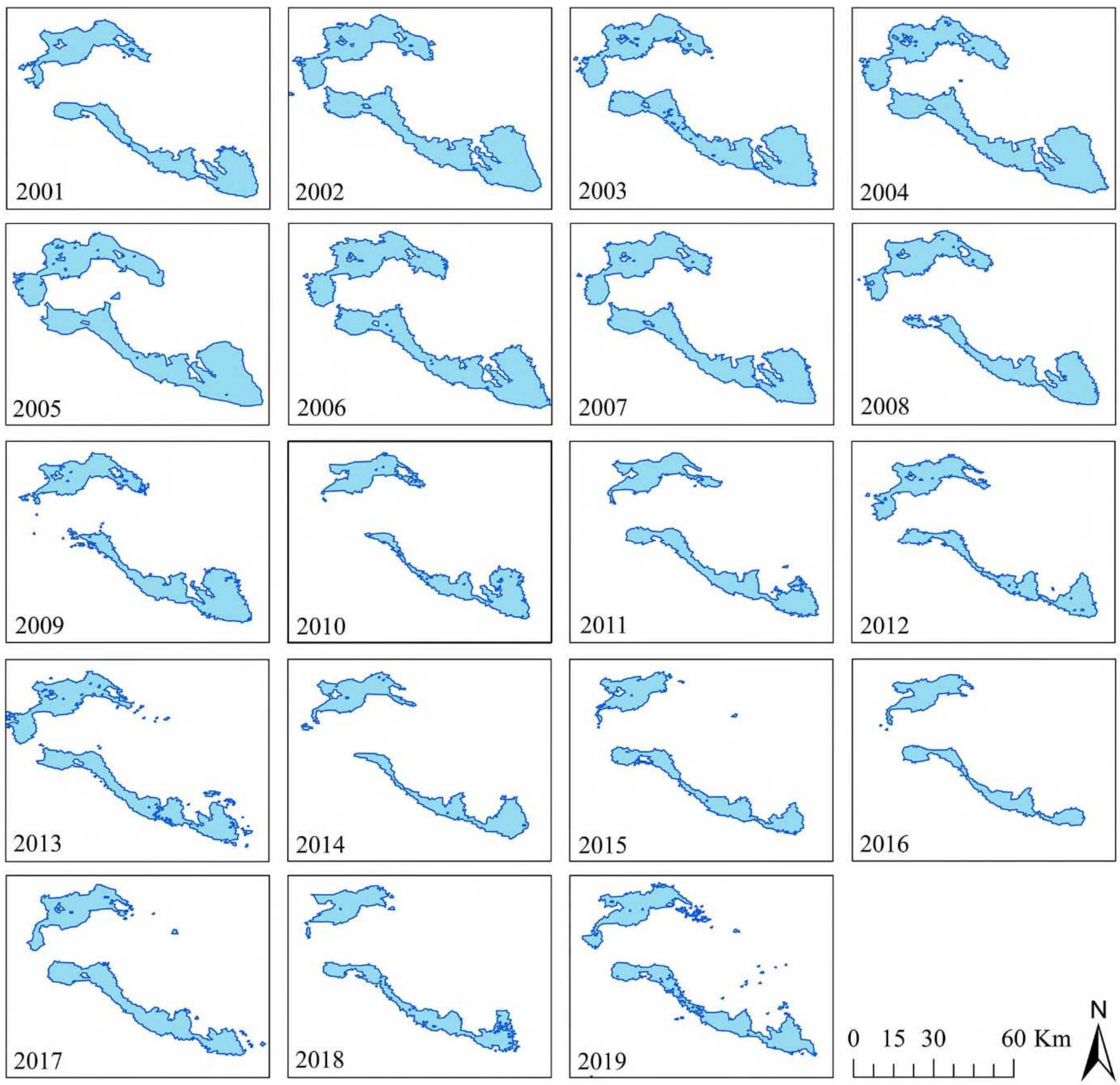

Fig. 8. Lake Surface changes per square kilometres from 2001 to 2019 based on MODIS satellite imagery.

The results obtained from the annual changes in surface area of TB Lakes are shown in Fig. 9. Surface area changes have decreased dramatically from 2001 to 2019, reaching 709.487 km^2 in 2001. In 2002, the A_L reached 975.64 km^2, which shows a 37% increase compared to 2001. In 2003, the lake's surface reached 821.55, and in 2004 and 2005, its value reached the highest level among the study years, occupying 1038.47 km^2 and 1088.07 km^2, respectively. After that, with a steep slope, the lake's surface shows a decrease until 2010 and this year it has reached 481.1 km^2. This indicates that between 2005 and 2010, the average level of lake decline was 11.16% per year. In 2011, there was an increase of 74.74 km^2 in the lake's water level and it fluctuated in the same range until 2013, and in 2014, it decreased by 132.192 km^2 compared to 2013, reaching 425,238 km^2. With an increase and cache, it reached 389.245 km^2 in 2016, which is the lowest number of observations among the study years. In 2017, the A_L shows an increase of 34.26%, and in 2018 and 2019, it has reached 379,158 and 480,937 km^2, respectively.

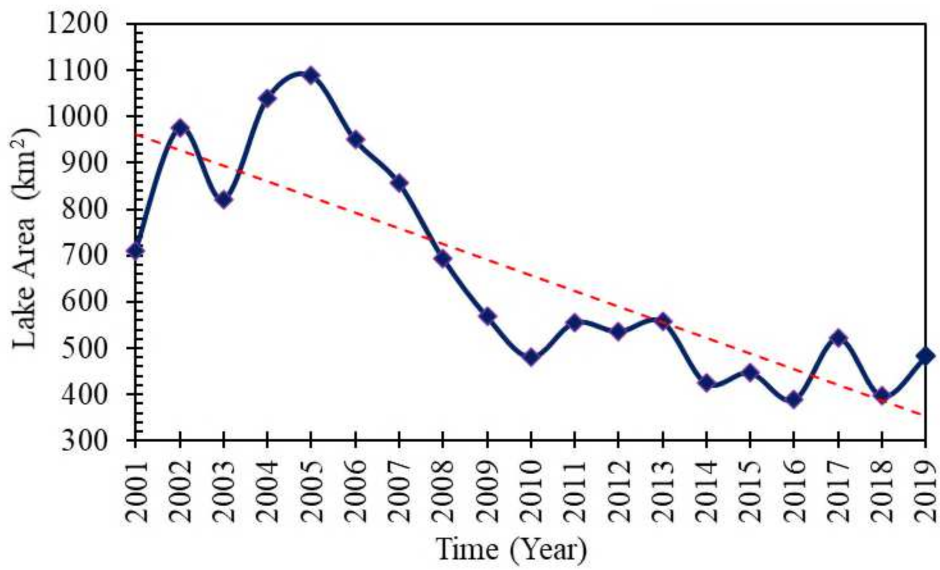

Fig. 9. Annual changes in the surface area of TB lakes (2000-2019)

Differences in the A_L between the study years confirm the information provided in the case study and can be considered as the main factor in reducing the water level of TB Lakes and changes in the region's ecosystem. Therefore, it is necessary to provide practical and correct solutions in the region to control the ecosystem and prevent further destruction of water resources in the region. Using applied models, the water level of TB Lakes can be modeled for better management in the future.

3.2. Obtained A_L time series attributes and pre-processing

The obtained A_L time-series statistical characteristics were investigated and the results are presented in Fig. 10. To survey the characteristics of the series and model it, the A_L series is divided into train and test parts with 70-30% ratio. From the 224 obtained data points, 157 (from Dec 2000 to Jul Dec 2013) and 67 (from Jan 2014 to Jul 2019) were considered as train and test parts, respectively (Fig. 10a). Regarding the information provided in Table 3 the statistical features of the intervals differ considerably, which can lead to poor modelling results.

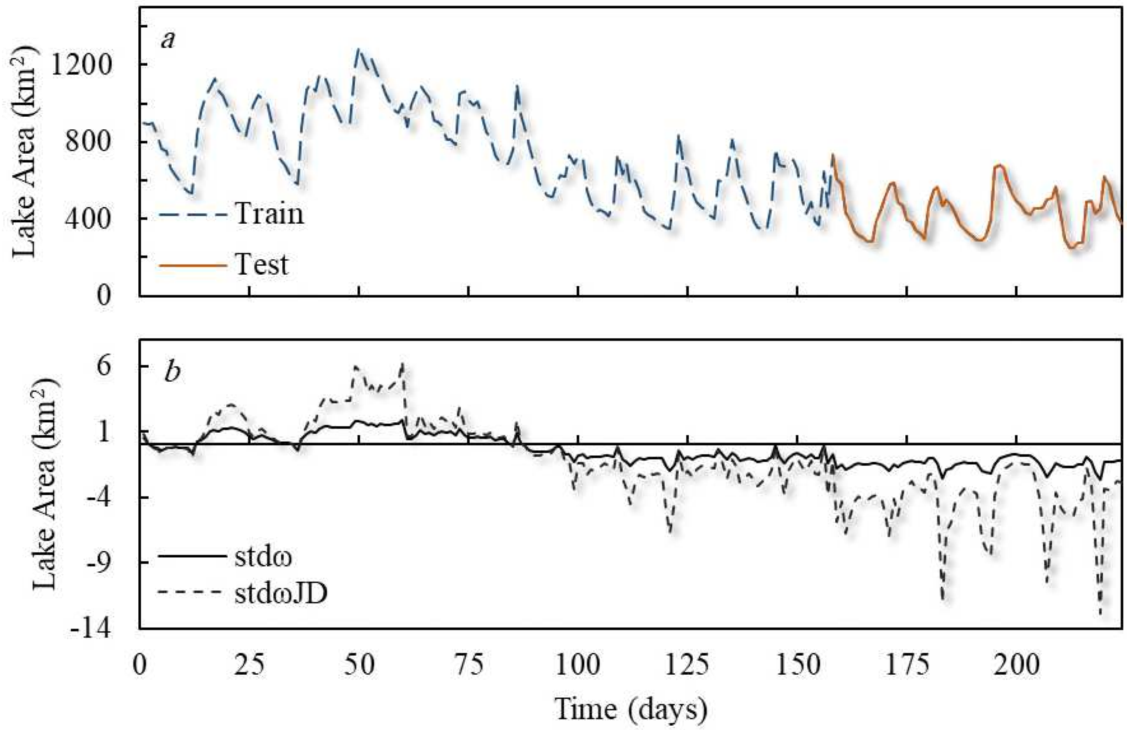

Fig. 10. (a) A_L time series plot and (b) pre-processed data.

According to the information provided in Table 3, the highest A_L lakes is 1292.32 km^2 which is related to Jan 2005 and the lowest value is related to 246.4 which is related to Jul 2018. The minimum values for train and test data are 342.52 km^2 and 246.4 km^2, respectively, and the maximum values for these two are 1292.32 km^2 and 733.39 km^2. The average value obtained for 224 data is 662.81 km^2 and in the train and test stage it is 757.44 and 441.08 km^2, respectively, and all data have positive skewness.

Table 3. Statistical attributes of Lakes Area (A_L) data

	Nbr.	Min (km^2)	Max (km^2)	1st Q (km^2)	Median (km^2)	3rd Q (km^2)	Mean (km^2)	σ (n)	γ_1	γ_2
Total	224	246.40	1292.32	455.76	605.36	882.24	662.81	256.94	0.42	-0.91
Train	157	342.52	1292.32	552.88	735.43	959.65	757.44	241.71	0.08	-1.08
Test	67	246.40	733.39	340.48	451.91	503.65	441.08	116.90	0.30	-0.58

Nbr., Number of data; Min. and Max., Minimum and Maximum of data; 1st Q. and 3rd Q., first and third Quarters; σ(n), Standard Deviation; γ1, Skewness; γ2, Kurtosis.

The results of the application of statistical tests to the A_L time series are provided in Table 4 and Fig. 10. According to MW, MK, SMK, KPSS tests results, the series has jumps and trends and is highly non-stationary. Furthermore, the JB test confirms the non-normality of the data. Therefore, pre-processing of A_L time series, prior to AI and stochastic modeling is mandatory.

The ACF and PACF values were calculated and the corresponding results are presented in Fig. 11 and Fig. 12. The plots plainly demonstrate the non-seasonal and seasonal trends and periodicity with lag 12. The periodicity is also observable in the time series plot (Fig. 10a) as iterative peaks and lows. This lake area data component was foreseeable as the surface water is highly impacted by solar energy's seasonal flux and earth's revolutions. Though this periodicity damped after two significant lags, the AL series would be more independent and better results can be obtained by removing it.

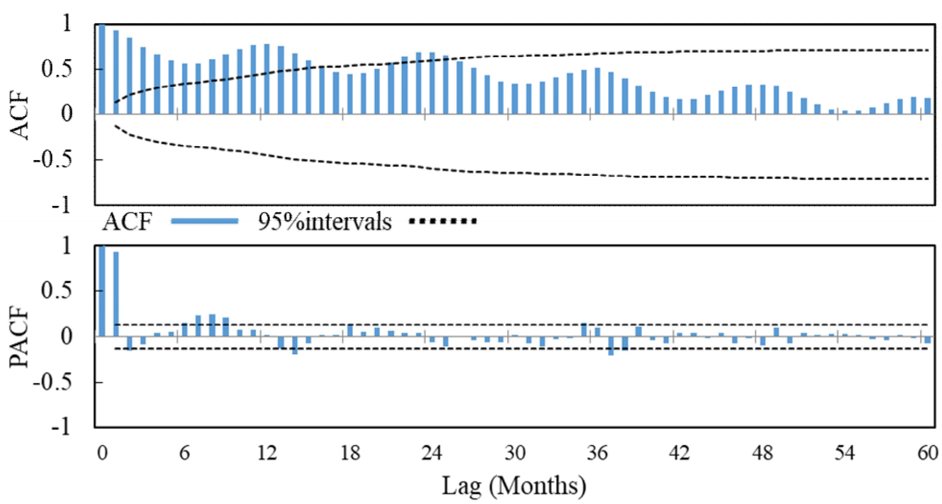

Fig. 11. A_L time series ACF and PACF plots.

For removing non-stationarity factors, the stdω method (stdω (A_L)) was applied to the series (Fig. 10b). After modeling, it was observed that this method only reduced the seasonality to one lag in the series and did not affect other terms. Since the stdω method contained the seasonal parameters, it was expected that it would affect mostly seasonal components. The JB transform was subsequently applied (stdωJD (A_L)). The normalization method was able to decrease the JB statistic markedly and normalize data. Also, normalization resulted in a reduction of the non-seasonal correlations from 22 to 18 lags. The corresponding results are presented in table 4 and Fig. 12 for each step.

Table 4 Lakes Area (A_L) time-series stationarity and normality tests outcomes

Tests	Jump	Trend		Stationarity	Norm.
	P_{MW}	P_{MK}	P_{SMK}	P_{KPSS}	JB*
A_L	0	0.01	0.01	0.01	7.72
stdω(A_L)	0.01	0.01	0.01	0.01	10.36
stdωJD(A_L)	0.01	0.01	0.01	0.01	2.15
Cons. Diff.**	81.21	53.36	37.30	98.02	1.33

*JB critical :5.99 ; p-value > 5% = acceptable; ** Consecutive 1st order non-seasonal and seasonal differencing

3.3. LSTM Deep learning modelling

Almost all the hydrological time series, regarding their nature, have a complex structure. Therefore, studying and involving historical events in the modelling process is of high importance. The LSTM model is an enhanced model produced to cover recurrent neural networks' deficiencies (RNN). The RNNs were limited in using historical data. However, the LSTM model unlimitedly can use long-term dependencies in modelling process.

Given the seasonal correlations in time series with lag 12, the LSTM model was used for modeling pre-processed data with the hidden cell states of h = 12, 60, 144 and 156 [45,89]. A piecewise learning rate schedule with Initial learn rate of 0.005 was defined for the model structure. After determining the maximum epochs of 500 and learn rate drop period and drop factor of 125 and 0.2, respectively, the single LSTM layer model was defined. Computational requirements represent an important consideration. In this work, the MATLAB software and a computer with a configuration of CPU core i7, 2500 MHz and 8G RAM were used. The average time spent for modeling each input was around 100 seconds. The results of the models are provided in Table 5. The LSTM model with the seasonal standardized (stdω) data and 12 inputs produced better results than inputs with higher hidden cell states with the same preprocessing.

Table 5 LSTM results for Lake Area (A_L) time series

Method	Inputs	R	RMSE	MAE	MAPE	RMSRE	U^I	U^{II}
stdω	**h12**	0.786	**113.227**	**92.001**	**0.230**	**0.289**	**0.114**	**0.248**
stdω	h60	**0.790**	144.837	124.816	0.317	0.380	0.140	0.317
stdω	h144	0.769	181.314	164.596	0.418	0.483	0.169	0.397
stdω	h156	0.746	200.116	183.361	0.465	0.532	0.184	0.439
stdωJD	**h12**	0.806	**109.140**	**91.571**	**0.229**	**0.281**	**0.110**	**0.239**
stdωJD	h60	**0.893**	116.363	104.381	0.263	0.304	0.115	0.255
stdωJD	h144	0.770	157.532	138.723	0.352	0.416	0.151	0.345
stdωJD	h156	0.852	146.578	132.055	0.331	0.380	0.141	0.321

h = hidden states no.

In the stdω method, except for h60, where the value of R is improved by 2% and h12 has a better performance in other statistical parameters, and as the number of inputs increases, the accuracy of the model is affected. h156 has the highest error values so that the correlation coefficient has decreased by 5% compared to h12 and the RMSE has increased by 76.7%. RMSRE and MAPE, have increased by more than 100%. These values for LSTM models demonstrated that the models' power and quality were higher while 12 inputs were chosen for modeling, compared to the other models with more inputs. Also, it indicates that the impact of most recent historical data is more than the oldest ones. This refers to the capability of the LSTM in modeling dependent data.

For further investigation, the pre-processed series with stationarization and normalization (stdωJD) were also modeled. Likewise, the LSTM model with 12 inputs produced the best results. The $LSTM_{std\omega JD}$ (12) indices are as R = 0.806, RMSE = 109.140, MAE = 91.571, MAPE = 0.229, RMSRE = 0.281, U^{I} = 0.110, U^{II} = 0.239. The Theil's coefficient also shows slight improvement in the model's quality and power while using normalization and standardization, compared to the single standardization.

The results show that in stdωJD, as in stdω, the model's accuracy decreases with increasing inputs. In h156 the value of the correlation coefficient is higher than h12 and h144. However, the statistical parameters show better performance for h12 compared to stdωJD model with other hidden cell inputs. As seen in the preprocessed data's correlogram, the seasonal correlation was damped after one seasonal lag and the dependencies were important up to one seasonal lag and few more non-seasonal lags. Therefore, the LSTM models with historical data up to previous 12 lags were invistigated. Moreover, the normalization of data distribution enhanced the modeling results and decreased the errors in comparison to lone standardization. The $LSTM_{std\omega JD}$ improved the results by R = 2.458%, RMSE = 3.610%, MAE = 0.468%, MAPE = 0.451%, RMSRE = 2.720%, U^{I} = 3.428%, U^{II} = 3.610%. This improvement proves the importance of the pre-processing in AI models, regardless of their capability in modeling non-linearity.

The structure of data should be investigated prior to the preprocessing to assess the impacts of the preprocessing methods. Also, it can be concluded that using more independent inputs causes more variations that impact the final results of the deep learning method. So, limiting the LSTM model inputs to the correlated data is important.

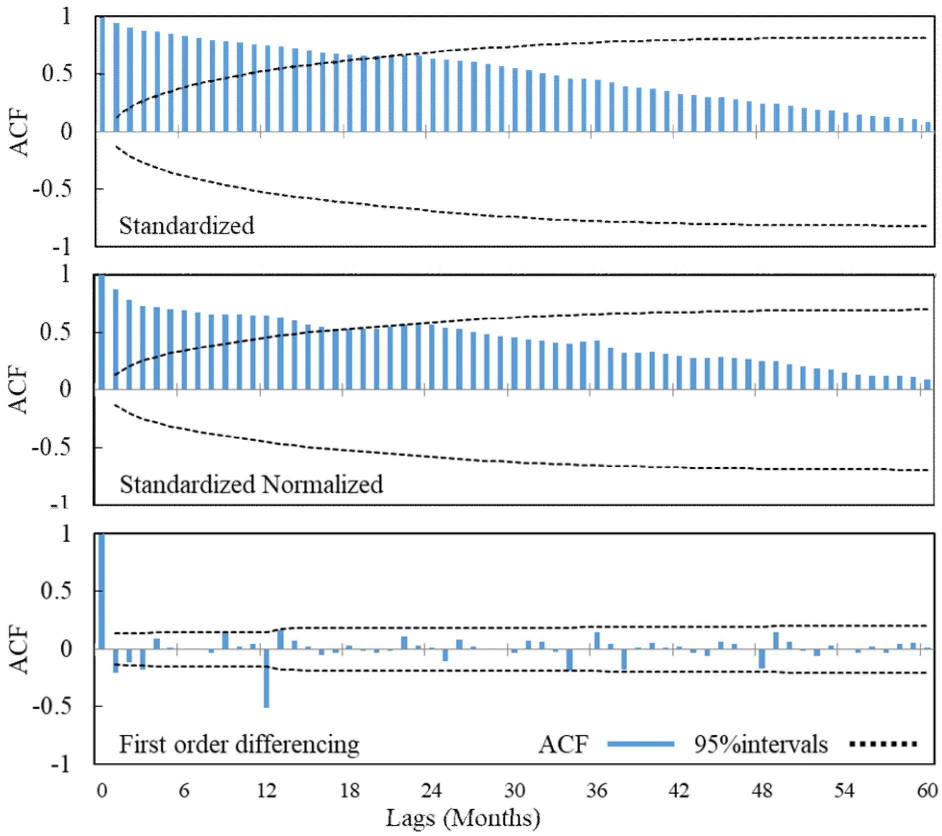

Fig. 12. A_L pre-processed time series ACF plots.

3.4. Stochastic modeling

Stochastic models are among the most conventional modelling methods in hydrology. These models are noticed for their simple theory and application. As the basis of these models are statistical concepts, some prerequisites should be considered in modelling process. The stationarity and normalization of time series are the two necessities of stochastic models. Concerning the results provided in section 3.2, as the pre-processed data's ACF values are damped after 18 lags and series is normal, modelling can be carried out, but higher orders of parameters are needed. Hence, a consecutive non-seasonal and seasonal differencing was applied to series, and it was observed that all non-stationarity factors were removed from series and became stationary. The corresponding results are presented in Table 4 and Fig. 12 for each step.

The correlations in ACF plots after consecutive differencing declines considerably to one lag. But for further survey of the model's capability, the orders of the parameters in SARIMA model are considered as: p = q = P = Q = {0, 1, 2, 3, 4, 5} and d = D = {0, 1} and seasonality ω = 12. After coding the dynamic model in MATLAB software and considering this parameter selection, a total number of 2590 models were produced with the same computer configuration used for the LSTM models. The time spent on stochastic modeling was about two hours. The minimum values of the indices for forecasted A_L data in all were R = 0.01, RMSE = 68.70, MAE = 49.42, MAPE = 0.11, RMSRE = 0.14, AICc = 574.80, UI = 0.08, U^{II} = 0.15 and the maximum values were R = 0.85, RMSE = 780.61, MAE = 756.47, MAPE = 1.85, RMSRE = 1.98, AICc = 862.04, UI = 0.47, U^{II} = 1.71. With these specifications and after considering the independence of the results, simplicity and goodness of the fit of models, the superior model was chosen as SARIMA $(1,0,0)(0,1,1)^{12}$. The evaluation results for this model are: R = 0.819, RMSE = 70.217, MAE = 49.425, MAPE = 0.106, RMSRE = 0.143, AICc = 574.82, UI = 0.077, U^{II} = 0.154. The model is the most parsimonious and adequate SARIMA model compared to the other 2589 models. It is observed that the model's correlation index is almost in the same range as the LSTM, but other indices like RMSE, MAPE are almost half. This means the linear model could forecast the variation of the AL data better than sole LSTMs after triple preprocessing and removing all the dependencies in the data. However, other model evaluation criteria should be investigated, and there are still opportunities for enhancements. Another step in the evaluation of stochastic modelling is checking the independence of the residuals. This criterion is assessed simultaneously with parsimony and other statistics to obtain a model which is not only precise but also has uncorrelated residuals. Therefore, the Ljung-Box test was applied to the stochastic model's residuals for 60 non-seasonal or five seasonal lags. The test indicated the independence of the residuals and the adequacy of the model. The results of the independence test for the superior model are provided in Fig. 12.

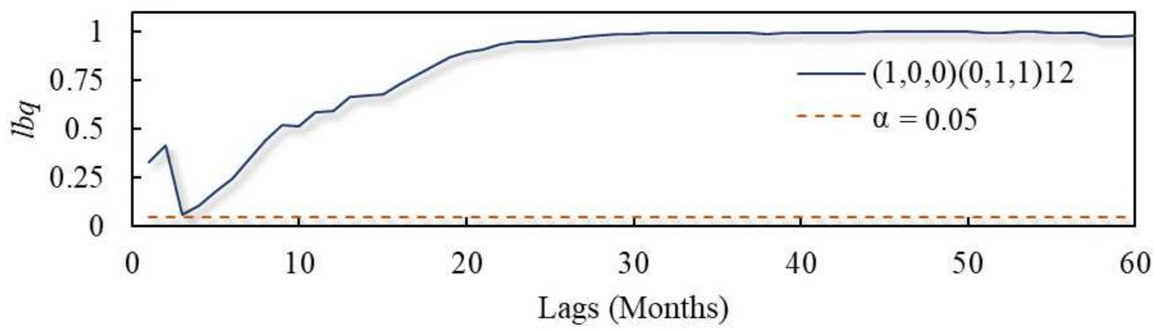

Fig.13. Ljung-Box residuals test results.

3.5. Hybrid Deep-learning-Stochastic modelling and disparities

Hybridization of models is one of the methods of utilizing non-linear and linear models' characteristics simultaneously. These methods allow researchers to model data and make predictions by covering the drawbacks of the single models and produce results with lower errors. For this purpose, the linear model residuals that are independent are used as inputs of the AI model. This input is assumed to be the non-linear part of the time series as the stochastic model is also assumed to be able to forecast the linear part [90]. As it can be seen in Fig. 14. The residuals of the linear model are completely independent, and no correlation remains in the residuals. However, they have the circumstances to be modeled by the AI model. Since, no correlation is found in the residuals' series, the AI model requires less inputs to forecast future steps. However, the previous steps will be followed to provide comparison circumstances.

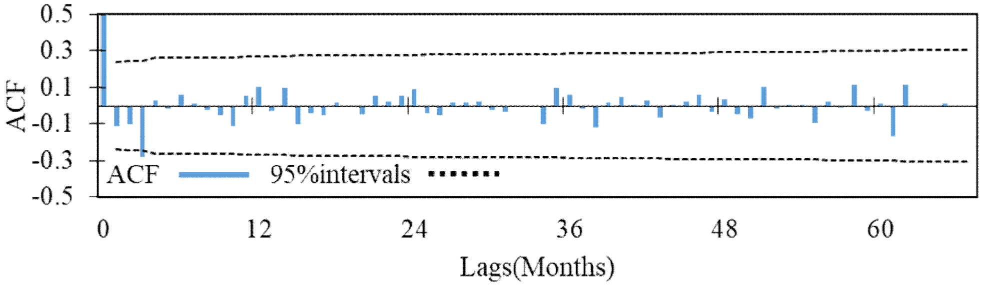

Fig. 14. Stochastic model residuals auto correlation function plot

B integrating SARIMA and LSTM, the superior linear model's residuals were modelled by the LSTM model with the same inputs considered for modelling in previous sections. The residuals are denoted as $SARIMA_s$. The results of the models are provided in Table 6. The SARIMAs-LSTM with 12 inputs outperformed other $SARIMA_s$-LSTM hybrid models. As shown in Fig. 14, the residuals do not have correlations, therefore, the best results with the 12 inputs were expected. Using hidden cells' inputs less than 12 could also produce these results.

Table 6 Hybrid models results for Lakes Area (A_L) time series

Method	Inputs	R	RMSE	MAE	MAPE	RMSRE	U^{I}	U^{II}
SARIMAs - LSTM	**h12**	**0.819**	**70.428**	**49.310**	**0.105**	**0.143**	**0.077**	**0.154**
	h60	0.777	79.138	60.137	0.131	0.165	0.087	0.173
	h144	0.754	100.928	82.246	0.198	0.243	0.104	0.221
	h156	0.752	104.037	85.689	0.208	0.252	0.107	0.228

h = hidden states no.

By comparing the results of the hybrid model and previously presented models, it was observed that the hybridization improved a few characteristics of the results. Compared to the single LSTM models, the Hybrid model increases the correlation of the forecast. It improved the mediation of the data by 0.061 compared to the average of the LSTM models. Also, the error indices were almost reduced to half. However, this improvement, compared to the linear model was less noticeable than lone LSTM models. The hybridization, on the other hand, lowered the MAPE and MAE indices.

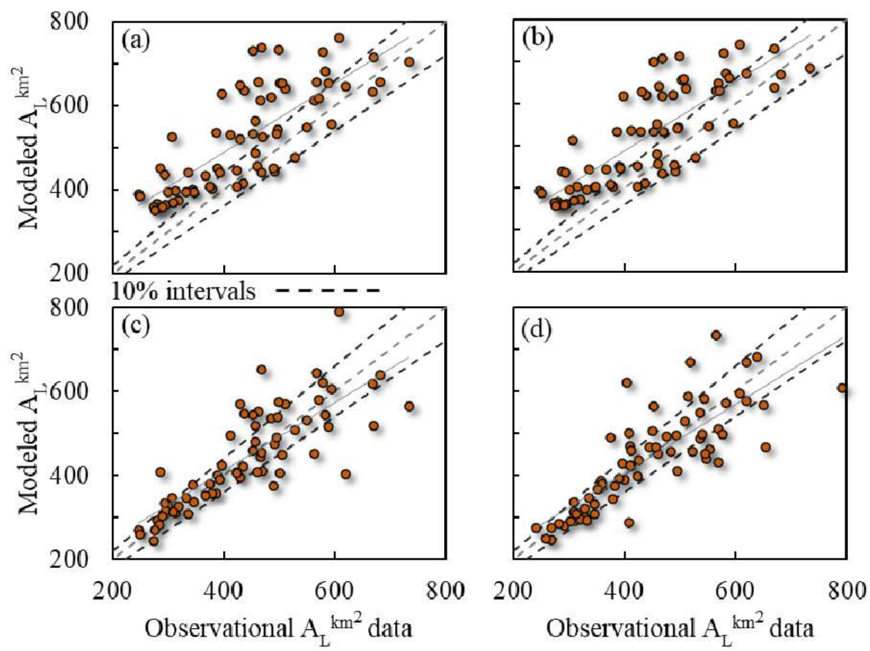

Fig.15. Scatter plots of the modeled A_L time series. a: $LSTM_{Std\omega}$ (h12); b: $LSTM_{Std\omega JD}$ (h12); c: SARIMA(1,0,0)(0,1,1)12; d: $Hybrid_S$ (h12).

Since the indices are very close and for better comparison, the scatter plots of the superior LSTM, SARIMA, and hybrid models are provided in Fig. 15. From the scatter plots, the dispersion of the modelled data can be observed. The LSTM models predicted data are more dispersed than SARIMA and hybrid models, respectively (Fig. 15 a and b). The linear model (Fig. 15c) has densified the data and brought it closer to the 10% range. However, the hybrid model was more successful than the others in bringing the forecasts closer to the median line and locating data in the 10% intervals (Fig. 15d). In other words, hybridization caused more correlation in the forecasted data and better mediation has occurred by utilizing both methods' characteristics. The Box plot of the observed data and superior models are drawn in Fig. 16, and it can be observed that the SARIMA (1, 0, 0) $(0, 1, 1)_{12}$ and $SARIMA_S$-LSTM model perfectly forecasted the interquartile area of the A_L time series and even were able to forecast one of the extreme values of the original series. These methods also predicted the maxima and minima of the data more accurately than other models. A potent model regenerates the statistical characteristics of the studied data. Though the linear model and the hybrid indices were slightly similar, the hybrid SARIMA-LSTM reproduced the primal statistical properties of WSA data better than sole models [91]. The hybrid model performed better in forecasting the mean and other statistical characteristics of the observed data slightly better than the SARIMA model. Therefore, hybridization was not able to produce noticeable results (Tables 5 and 6) but reproduced the original series statistical attributes. Thus, it can be considered as a superior WSA modelling methodology.

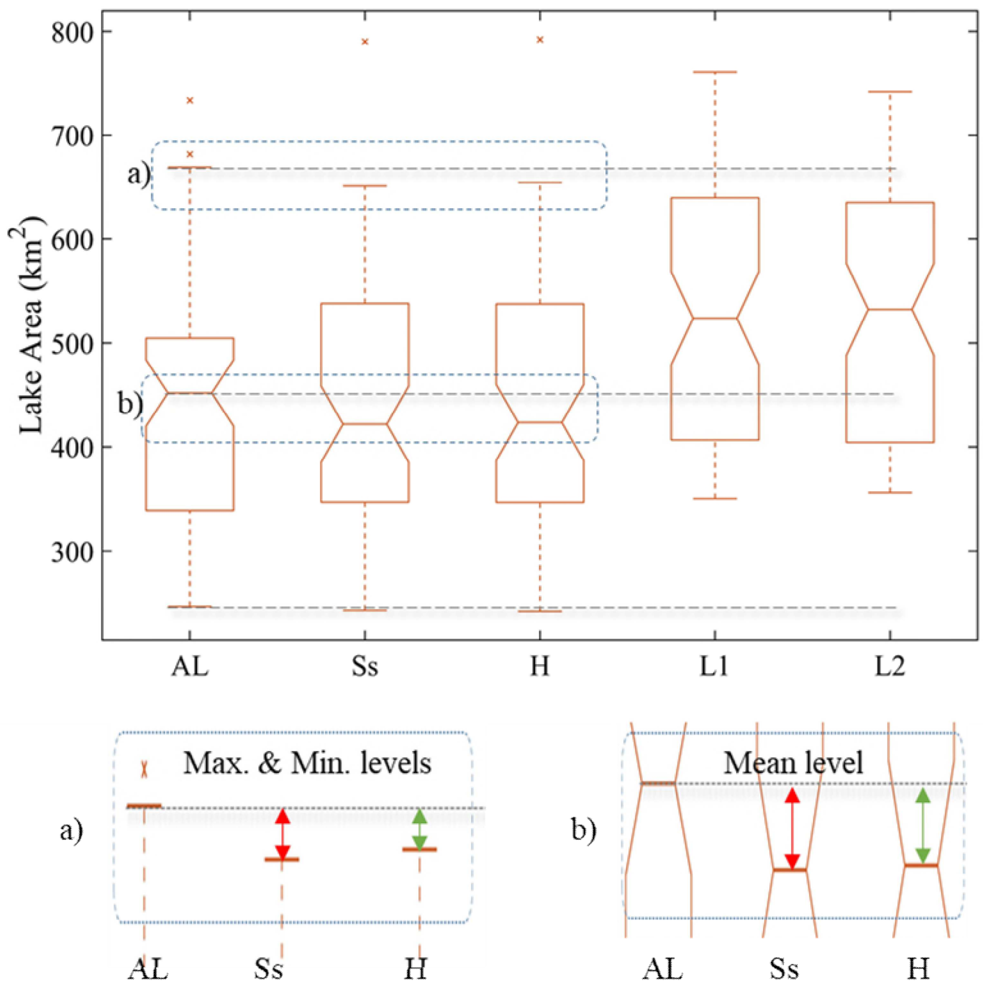

Fig. 16. Box plot of the superior models; AL: observed WSA data, Ss: SARIMA (1, 0, 0) (0, 1, 1)$_{12}$; H: SARIMA$_S$-LSTM; L1: LSTM$_{std\omega JD}$ (12), L2: LSTM$_{std\omega JD}$ (12);

4. Conclusion

Sustainable management of freshwater inland lakes in an arid region plays a vital role in environmental preservation and quality of life. Moreover, monitoring changes in the lake's surface area due to both natural and anthropogenic stressors helps to better plan and manage water resources. Therefore, the accurate mapping and monitoring of lake surface area, and the forecasting of these vital resources future trends are of great importance for planning and management purposes. In this study, the WSA of the TB lakes is studied. To map the lake's surface area, the MODIS satellite images were used to extract a time series depicting changes of the WSA. The images were obtained from MODIS data, MOD09A1 version 6. The pre-processing of the images included image preparation, classification, and statistical computation. The preparation and classification of the images were undertaken in GEE environment. Using the MNDWI index, the water mass was separated from the background, and the lake area was obtained from the chosen images. Finally, by repeating the process for images from 2001 to 2019 a monthly time series of lakes areas (A_L) was obained. The A_L time series was examined by stationarity and normality tests to investigate the structure of the timeseries. Periods with 12 lag repetition, trends and jumps with a non-normal distribution were observed in the timeseries. The timeseries was pre-processed with the conventional seasonal standardization (stdω) method and normalized with the John-Draper (JD) transform, two-time series were obtained.

These timeseries were modelled with the LSTM model with h = {12, 60, 144, 156} number of hidden cell states. The single LSTM models, with the two different preprocessing tasks, required only 12 hidden cell states to obtain the highest accuracy. $LSTM_{std\omega}$ (12) with R = 0.786, RMSE = 113.227, MAPE = 0.230 and $STM_{std\omega JD}$ (12) with R = 0.806, RMSE = 109.140, MAPE = 0.229 outperformed others. These results indicated that using multiple preprocessing methods and reevaluating the results of the time series structure tests is necessary since most of the time, the latter part is neglected in the AI modeling procedure.

A stochastic SARIMA model and hybridization of both deep learning and stochastic models were carried out for further investigation and surveying the possibilities to enhance the forecasting results. The superior linear model was chosen as SARIMA with (1, 0, 0) (0, 1, 1)12 parameters based on goodness of fit and model parsimony. The stochastics models' results were better than single LSTM models and the errors were reduced by almost half, R = 0.819, MAE = 49.425, MAPE = 0.106. To utilize both models’ capabilities, residuals of the stochastic model were modelled by LSTM.

Results indicate that the hybrid model indices were marginally better than others,. The scatter and Box plots of the models revealed that the hybridization did not produce noticeable better error indices but improved the statistical characteristics and made them closer to observational data. The hybrid SARIMA-LSTM reproduced the primal statistical properties of WSA data and caused better mediation as observed in scatter plots and the Box plot of the data compared to sole models.

In conclusion, the hybridization can reproduce model forecasts that better preserve the observed timeseries's statistical attributes compared to single models. Therefore, it is suggested that the undertaken methodology of A_L time series modelling be applied to other A_L time series and other AI methods like Extreme Learning Machine (ELM), LSTM developments like Genetic Algorithm (GA)-LSTM and a combination of these models with linear models be investigated.

5. References

[1] Yamazaki D, Trigg, MA, Ikeshima D (2015) Development of a global~ 90 m water body map using multi-temporal Landsat images. Remote Sens. Environ 171:337-351. https://doi.org/10.1016/j.rse.2015.10.014.

[2] Santoro M, Wegmüller U, Lamarche C, Bontemps S, Defourny P, Arino O, (2015) Strengths and weaknesses of multi-year Envisat ASAR backscatter measurements to map permanent open water bodies at global scale. Remote Sens. Environ 171:185–201. https://doi.org/10.1016/j.rse.2015.10.031.

[3] Masocha M, Dube T, Makore M, Shekede, MD, Funani J, (2018) Surface water bodies mapping in Zimbabwe using landsat 8 OLI multispectral imagery: A comparison of multiple water indices. Phys. Chem. Earth 106:63–67, https://doi.org/10.1016/j.pce.2018.05.005.

[4] Rishikeshan CA, Ramesh H (2018) An automated mathematical morphology driven algorithm for water body extraction from remotely sensed images, ISPRS J. Photogramm. Remote Sens 146:11–21. https://doi.org/10.1016/j.isprsjprs.2018.08.014

[5] Huovinen P, Ramírez J, Caputo L, Gómez I (2019) Mapping of spatial and temporal variation of water characteristics through satellite remote sensing in Lake Panguipulli, Chile, Sci. Total Environ. 679:196–208. https://doi.org/10.1016/j.scitotenv.2019.04.367

[6] A Haghighi AT, Kløve B (2015) A sensitivity analysis of lake water level response to changes in climate and river regimes, Limnologica 51 118–130. https://doi.org/10.1016/j.limno.2015.02.001.

[7] Nkhonjera GK (2017) Understanding the impact of climate change on the dwindling water resources of South Africa, focusing mainly on Olifants River basin: A review, Environ. Sci. Policy 71:19–29. https://doi.org/10.1016/j.envsci.2017.02.004

[8] Motew M, Chen X, Carpenter S.R, Booth EG, Seifert J, Qiu J, Loheide II SP, Turner MG, Zipper SC, Kucharik CJ (2019) Comparing the effects of climate and land use on surface water quality using future watershed scenarios. Sci. Total Environ 693:133484. https://doi.org/10.1016/j.scitotenv.2019.07.290

[9] Sinyukovich VN, Chernyshov MS (2019) Water regime of lake Baikal under conditions of climate change and anthropogenic influence. Quat. Int. 524:93–101. https://doi.org/10.1016/j.quaint.2019.05.023.

[10] Sheklabadi M, Mahmoudzadeh H, Mahboubi AA, Gharabaghi B, Ahrens B (2015) Long-term land-use change effects on phosphorus fractionation in Zrêbar Lake margin soils, Arch. Agron. Soil Sci 61 737–749. https://doi.org/10.1016/j.quaint.2019.05.023

[11] Sima S, Tajrishy M (2013) Using satellite data to extract volume–area–elevation relationships for Urmia Lake, Iran, J. Great Lakes Res 39:90–99. https://doi.org/10.1016/j.jglr.2012.12.013.

[12] Xu H (2006) Modification of normalised difference water index (NDWI) to enhance open water features in remotely sensed imagery. Int. J. Remote Sens 27:3025–3033. https://doi.org/10.1080/01431160600589179

[13] Klein I, Dietz A, Gessner U, Dech S, Kuenzer C (2015) Results of the Global WaterPack: A novel product to assess inland water body dynamics on a daily basis, Remote Sens. Lett 61:78–87. https://doi.org/10.1080/2150704X.2014.1002945

[14] Soltani K, Amiri A, Zeynoddin M, Ebtehaj I, Gharabaghi B, Bonakdari H (2021) Forecasting monthly fluctuations of lake surface areas using remote sensing techniques and novel machine learning methods. theor appl climatol 143:713-735. https://doi.org/10.1007/s00704-020-03419-6

[15] Ben-Romdhane H, Al-musallami M, Marpu PR, Ouarda TB MJ. Ghedira H (2018). Change detection using remote sensing in a reef environment of the UAE during the extreme event of El Niño 2015–2016, Int. J. Remote Sens: 1-25. https://doi.org/10.1080/01431161.2018.1460502

[16] Alobaidi MH, Marpu PR, Ouarda TB MJ, Ghedira H (2014). Mapping of the solar irradiance in the UAE using advanced Artificial Neural Network Ensemble. IEEE J Sel Top Appl 7: 3668-3680. https://doi.org/10.1109/JSTARS.2014.2331255, 3668-3680

[17] Soltani K, Ebtehaj I, Amiri A, Azari A, Gharabaghi B, Bonakdari H (2021) Mapping the spatial and temporal variability of flood susceptibility using remotely sensed normalized difference vegetation index and the forecasted changes in the future. Sci. Total Environ 770, 145288. https://doi.org/10.1016/j.scitotenv.2021.145288

[18] Gorelick N, Hancher M, Dixon M, Ilyushchenko S, Thau D, Moore R (2017),Google Earth Engine: Planetary-scale geospatial analysis for everyone, Remote Sens. Environ. 202:18–27, https://doi.org/10.1016/j.rse.2017.06.031

[19] Hansen E, Panwar R, Vlosky R (2013) the Global Forest Sector: Changes, Practices, and Prospects, Boca Raton, Taylor and Francis.

[20] Lobell DB, Thau D, Seifert C, Engle E, Little B (2015) A scalable satellite-based crop yield mapper, Remote Sens. Environ. 164:324–333. https://doi.org/10.1016/j.rse.2015.04.021

[21] Liosis N, Marpu PR, Pavlopoulos K, Ouarda TB MJ (2018) Ground subsidence monitoring with SAR interferometry techniques in the rural area of Al Wagan, UAE, Remote Sensing of Environment. 216:276-288. https://doi.org/10.1016/j.rse.2018.07.001

[22] Ben-Romdhane H, Marpu PR, Ouarda, TB MJ, Ghedira H (2016) Corals & benthic habitat mapping using DubaiSat-2: a spectral-spatial approach applied to Dalma Island, UAE, Remote Sensing Letters. 7:781-789. https://doi.org/10.1080/2150704X.2016.1187317

[23] Pekel JF, Cottam A, Gorelick N, Belward AS (2016) High-resolution mapping of global surface water and its long-term changes, Nature. 540 418–422. https://doi.org/10.1038/nature20584.

[24] Gonzalez R, Ouarda TB MJ, Marpu PR, Allam M., Eltahir EAB, Pearson S (2016) Water Budget Analysis in Arid Regions, Application to the United Arab Emirates. Water, 8:415. https://doi.org/10.3390/w8090415

[25] Beaton A, Whaley R, Corston K, Kenny F (2019) Identifying historic river ice breakup timing using MODIS and Google Earth Engine in support of operational flood monitoring in Northern Ontario, Remote Sens. Environ. 224:352–364, https://doi.org/10.1016/j.rse.2019.02.011

[26] Liu X, Hu G, Chen Y, Li X, Xu X, Li S, Pei F, Wang S (2019) High-resolution multi-temporal mapping of global urban land using Landsat images based on the Google Earth Engine Platform, Remote Sens. Environ. 209:227–239. https://doi.org/10.1016/j.rse.2018.02.055

[27] Lazzarini M, Molini A, Marpu PR., Ouarda TB MJ, Ghedira H (2015) Urban climate modifications in hot desert cities: The role of land cover, local climate, and seasonality, Geophysical Research Letters 42:9980-9989. https://doi.org/10.1002/2015GL066534

[28] Eissa Y, Marpu PR, Gherboudj I, Ghedira H, Ouarda TB MJ, and Chiesa M (2013) Artificial Neural Network Based Model for Retrieval of the Direct Normal, Diffuse Horizontal and Global Horizontal Irradiances using SEVIRI Images. Solar Energy. 89:1-16. https://doi.org/10.1016/j.solener.2012.12.008

[29] Klisch A, Atzberger C (2016), Operational drought monitoring in Kenya using MODIS NDVI time series. Remote Sens. 8:267. https://doi.org/10.3390/rs8040267

[30] Kong D, Zhang Y, Gu X, Wang D (2019) A robust method for reconstructing global MODIS EVI time series on the Google Earth Engine, ISPRS J. Photogramm. Remote Sens. 155:13–24. https://doi.org/10.1016/j.isprsjprs.2019.06.014

[31] Zaji AH, Bonakdari H, Gharabaghi B (2018) Applying upstream satellite signals and a 2-D error minimization algorithm to advance early warning and management of flood water levels and river discharge, IEEE Trans. Geosci. Remote Sens. 57:902–910, https://doi.org/10.1109/TGRS.2018.2862640

[32] Zaji, AH, Bonakdari H, Gharabaghi B (2018) Remote sensing satellite data preparation for simulating and forecasting river discharge, IEEE Trans. Geosci. Remote Sens. 56:3432–3441. 3441. https://doi.org 10.1109/TGRS.2018.2799901

[33] Zaji AH, Bonakdari H, Gharabaghi B (2019) Developing an AI-based method for river discharge forecasting using satellite signals, Theor. Appl. Climatol. 138:347–362. https://doi.org/10.1007/s00704-019-02833-9

[34] Moreira AA, Ruhoff AL, Roberti DR, de Arruda Souza V, da Rocha HR, de Paiva RCD (2019) Assessment of terrestrial water balance using remote sensing data in South America, J. Hydrol. 575:131–147. https://doi.org/10.1016/j.jhydrol.2019.05.021

[35] Bonakdari H, Moeeni H, Ebtehaj I, Zeynoddin M, Mahoammadian A, Gharabaghi B (2019), New insights into soil temperature time series modeling: linear or non-linear?, Theor. Appl. Climatol. 135 1157–1177. https://doi.org/10.1007/s00704-018-2436-2

[36] Ouarda TB MJ, Charron C, Marpu R, Chebana F (2016) The generalized additive model for the assessment of the direct, diffuse and global solar irradiances using SEVIRI images, with application to the UAE, IEEE J Sel Top Appl. 9:1553-1566. https://doi.org/10.1109/JSTARS.2016.2522764

[37] Nath RK, Deb S (2010) Water-body area extraction from high resolution satellite images-an introduction, review, and comparison. Int. J. Image Process. 3:265–384

[38] Abou El-Magd IH, Ali EM (2012) Estimation of the evaporative losses from Lake Nasser, Egypt using optical satellite imagery. Int. J. Digital Earth. 5:133–146. https://doi.org/10.1080/17538947.2011.586442

[39] Song C, Huang B, Ke L (2013) Modeling and analysis of lake water storage changes on the Tibetan Plateau using multi-mission satellite data, Remote Sens. Environ. 135:25–35. https://doi.org/10.1016/j.rse.2013.03.013

[40] Veh G (2019) Outburst floods from moraine-dammed lakes in the Himalayas (Ph.D. dissertation). University of Potsdam, Berlin Germany. https://doi.org/10.25932/publishup-43607

[41] Weiss L, Thé J, Winter J, Gharabaghi B (2018) Optimizing best management practices to control anthropogenic sources of atmospheric phosphorus deposition to inland lakes, J. Air Waste Manage. Assoc. 68 1025–1037. https://doi.org/10.1080/10962247.2018.1463929

[42] Kratzert F, Klotz D, Brenner C, Schulz K, Herrnegger M (2018) Rainfall–runoff modelling using long short-term memory (LSTM) networks, Hydrol. Earth Syst. Sci. 22:6005–6022. https://doi.org/10.5194/hess-22-6005-2018

[43] Langridge M, Gharabaghi B, McBean E, Bonakdari H, Walton R (2020) Understanding the dynamic nature of Time-to-Peak in UK streams. J. Hydrol. 583:124630. https://doi.org/10.1016/j.jhydrol.2020.124630

[44] Schmidhuber J (2015) Deep learning in neural networks: an overview, Neural Netw. 61:85–117. https://doi.org/10.1016/j.neunet.2014.09.003

[45] Kumar D, Singh A, Samui P, Jha RK (2019) Forecasting monthly precipitation using sequential modelling. Hydrol. Sci. J. 64 690–700. https://doi.org/10.1080/02626667.2019.1595624

[46] Ouali, D, Chebana F, Ouarda TB MJ. (2017) Fully nonlinear statistical and machine-learning approaches for hydrological frequency estimation at ungauged sites, Journal of Advances in Modeling Earth Systems. 9:1292-1306. doi:10.1002/2016MS000830

[47] Bahmani R, Ouarda TB MJ (2021), Groundwater level modeling with hybrid artificial intelligence techniques, J. Hydrol, 595, 125659. doi.org/10.1016/j.jhydrol.2020.125659

[48] Collobert R, Weston J, Bottou L, Karlen M, Kavukcuoglu K, Kuksa P (2011) Natural language processing (almost) from scratch, J. Mach. Learn. Res. 12:2493–2537

[49] Jiang M, Hou J, Yang C, Zhu X, Yin X (2019) Detecting Text in NeWSA Images with Similarity Embedded Proposals, Int. Conf. Doc. Anal. Recog. IEEE, 520-525. https://doi.org/10.1109/ICDAR.2019.00089

[50] Ha JH, Lee YH, Kim YH (2016) Forecasting the precipitation of the next day using deep learning, J. Korean Inst. Intelligent Systems. 26:93–98. https://doi.org/10.5391/JKIIS.2016.26.2.093

[51] Li X, Li Z, Huang W, Zhou P (2020) Performance of statistical and machine learning ensembles for daily temperature downscaling, Theor. Appl. Climatol. 140:571–588. https://doi.org/10.1007/s00704-020-03098-3

[52] Mohan AT, Gaitonde DV (2018) A deep learning based approach to reduced order modeling for turbulent flow control using LSTM neural networks, arXiv preprint arXiv:1804.09269

[53] Murad A, Pyun JY (2017) Deep recurrent neural networks for human activity recognition. Sensors. 17:2556, https://doi.org/10.3390/s17112556

[54] Sahoo BB, Jha R, Singh A, Kumar D (2019) Long short-term memory (LSTM) recurrent neural network for low-flow hydrological time series forecasting, Acta Geophys. 67:1471–1481. https://doi.org/10.1007/s11600-019-00330-1

[55] Moeeni H, Bonakdari H, Fatemi SE, Zaji AH (2017) Assessment of stochastic models and a hybrid artificial neural network-genetic algorithm method in forecasting monthly reservoir inflow, INAE Lett. 2:13–23. https://doi.org/10.1007/s41403-017-0017-9

[56] Sirangelo B, Caloiero T, Coscarelli R, Ferrari E (2017) A stochastic model for the analysis of maximum daily temperature, Theor. Appl. Climatol. 130:275–289. https://doi.org/10.1007/s00704-016-1879-6

[57] Zeynoddin M, Bonakdari H (2019) Investigating methods in data preparation for stochastic rainfall modeling: A case study for Kermanshah synoptic station rainfall data, Iran, J. appl. res. water wastewater. 6:32–38. https://doi.org/10.22126/ARWW.2019.1130

[58] Zeynoddin M, Bonakdari H, Ebtehaj I, Azari A, Gharabaghi B (2020) A generalized linear stochastic model for lake level prediction, Sci. Total Environ. 723:138015. https://doi.org/10.1016/j.scitotenv.2020.138015

[59] Papalaskaris T, Panagiotidis T, Pantrakis A (2016) Stochastic monthly rainfall time series analysis, modeling and forecasting in Kavala City, Greece, North-Eastern Mediterranean Basin, Procedia Eng. 162:254–263. https://doi.org/10.1016/j.proeng.2016.11.054

[60] Mombeni HA, Rezaei S, Nadarajah S, Emami M (2013) Estimation of water demand in Iran based on SARIMA models, Environ. Model. Assess. 18:559–565. https://doi.org/10.1007/s10666-013-9364-4.

[61] Moeeni H, Bonakdari H, Ebtehaj I (2017) Integrated SARIMA with neuro-fuzzy systems and neural networks for monthly inflow prediction. Water Resour. Manage. 31:2141–2156. https://doi.org/10.1007/s11269-017-1632-7

[62] Zeynoddin M, Bonakdari H, Azari A, Ebtehaj I, Gharabaghi B, Madavar HR (2018) Novel hybrid linear stochastic with non-linear extreme learning machine methods for forecasting monthly rainfall a tropical climate, J. Environ. Manage. 222:190–206. https://doi.org/10.1016/j.jenvman.2018.05.072

[63] Lotfi K, Bonakdari H, Ebtehaj I, Mjalli FS, Zeynoddin M, Delatolla R, Gharabaghi B (2019) Predicting wastewater treatment plant quality parameters using a novel hybrid linear-nonlinear methodology, J. Environ. Manage. 240:463–474. https://doi.org/10.1016/j.jenvman.2019.03.137.

[64] Ruiz-Aguilar JJ, Turias IJ, Jiménez-Come MJ (2014) Hybrid approaches based on SARIMA and artificial neural networks for inspection time series forecasting, Transport. Res. Part E: Logist. Transport. Rev. 67:1–13. https://doi.org/10.1016/j.tre.2014.03.009

[65] Mishra AK, Desai VR, Singh VP (2007) Drought forecasting using a hybrid stochastic and neural network model, J. Hydrol. Eng. 12:626–638. https://doi.org/10.1061/(ASCE)1084-0699(2007)12:6(626)

[66] Shafaei M, Adamowski J, Fakheri -Fard A, Dinpashoh Y, Adamowski K (2016) A wavelet-SARIMA-ANN hybrid model for precipitation forecasting, J. Water Land Dev. 28:27–36. https://doi.org/10.1515/jwld-2016-0003

[67] Sajedipour S, Zarei H, Oryan S (2017) Estimation of environmental water requirements via an ecological approach: A case study of Bakhtegan Lake, Iran, Ecol. Eng. 100:246–255. https://doi.org/10.1016/j.ecoleng.2016.12.023

[68] Haghighi AT, Menberu MW, Aminnezhad M, Marttila H, Kløve B (2016) Can lake sensitivity to desiccation be predicted from lake geometry?, J. Hydrol. 539:599–610. https://doi.org/10.1016/j.jhydrol.2016.05.064

[69] Abou Zaki N, Torabi Haghighi A, Rossi PM, Tourian MJ, Kløve B (2019) Monitoring Groundwater Storage Depletion Using Gravity Recovery and Climate Experiment (GRACE) Data in Bakhtegan Catchment, Iran, Water, 11:1456. https://doi.org/10.3390/w11071456

[70] Sehhatisabet ME, Musavi SB, Bakhtiari P, Moghaddas D, Hamidi N, Nezami B, Khaleghizadeh (2006) A Further significant extensions of migrant distribution and breeding and wintering ranges in Iran for over sixty species, Sandgrouse. 28:146–155.

[71] Scott DA, Rose P (1996) Atlas of Anatidae populations in Africa and Western Eurasia. Wetlands International Publication 41, Wetlands International, Wageningen, Netherlands

[72] Scott DA (2007) A review of the status of the breeding waterbirds in Iran in the 1970s, Podoces. 2:1–21.

[73] McFeeters SK (1996) The use of the Normalized Difference Water Index (NDWI) in the delineation of open water features, Int. J. Remote Sens. 17:1425–1432. https://doi.org/10.1080/01431169608948714

[74] Chew C, Small E (2020) Estimating inundation extent using CYGNSS data: A conceptual modeling study, Remote Sens. Environ. 246:111869. https://doi.org/10.1016/j.rse.2020.111869

[75] Pena-Regueiro J, Sebastiá-Frasquet MT, Estornell J, Aguilar-Maldonado JA (2020) Sentinel-2 Application to the Surface Characterization of Small Water Bodies in Wetlands, Water. 12:1487. https://doi.org/10.3390/w12051487

[76] Hamilton J.D (1994) Time Series Analysis, Vol. 2, Princeton university press Princeton

[77] Kwiatkowski D, Phillips PC, Schmidt P, Shin Y (1992) Testing the null hypothesis of stationarity against the alternative of a unit root, J. Econom. 54:159–178. https://doi.org/10.3390/w12051487

[78] Gebrekristos ST, Kassew A (2019) Hydrologic responses to land use/Land cover change in the Kesem Watershed, Awash basin, Ethiopia, J. Spat. Hydrol. 15:1–31

[79] Mann HB, Whitney DR (1947) On a test of whether one of two random variables is stochastically larger than the other, Ann. Math. Stat. 18:50–60

[80] Yue S, Wang CY (2002) Power of the Mann–Whitney test for detecting a shift in median or mean of hydro-meteorological data, Stochastic Environ. Res. Risk Assess. 16:307–323, https://doi.org/10.1007/s00477-002-0101-9

[81] Moeeni H, Bonakdari H (2017) Forecasting monthly inflow with extreme seasonal variation using the hybrid SARIMA-ANN model, Stochastic Environ. Res. Risk Assess. 31:1997–2010. https://doi.org/10.1007/s00477-016-1273-z

[82] Box GE, Jenkins GM, Reinsel GC, Ljung GM (2015) Time Series Analysis: Forecasting and Control, John Wiley and Sons, New Jersey

[83] Salas JD, Delleur JW, Yevjevich VM, Lane WL (1980) Applied Modeling of Hydrologic Time Series, Water Resources Publications, Littleton.

[84] Jarque CM, Bera AK (1980) Efficient tests for normality, homoscedasticity and serial independence of regression residuals, Econ Lett. 6:255–259

[85] Theil H (1961) Economic forecasts and policy, North Holland Publishing Company

[86] Theil H (1966) Applied economic forecasting, North Holland Publishing Company

[87] Burnham KP, Anderson DR (2002) Model selection and multimodel inference: a practical information-theoretic approach, Springer, New York

[88] Ljung GM, Box GE (1978) On a measure of lack of fit in time series models, Biometrika, 65:297–303, https://doi.org/10.1093/biomet/65.2.297

[89] Wu CL, Chau KW, Fan C (2010) Prediction of rainfall time series using modular artificial neural networks coupled with data-preprocessing techniques, J. Hydrol. 389:146–167. https://doi.org/10.1016/j.jhydrol.2010.05.040

[90] Moeeni H, Bonakdari H (2017) Forecasting monthly inflow with extreme seasonal variation using the hybrid SARIMA-ANN model. Stochastic environmental research and risk assessment. 31:1997-2010. https://doi.org/10.1007/s00477-016-1273-z

[91] Singh VP, Frevert DK (2002) Mathematical Models of Large Watershed Hydrology, Water Resources Publications, Highlands Ranch